

1 New constraints from Central Chile on the origins of enriched continental
2 compositions in thick-crustal arc magmas

3 Penny E. Wieser^{1,2*}, Stephen J. Turner³, Tamsin A. Mather¹, David M. Pyle¹, Ivan P. Savov⁴ and
4 Gabriel Orozco⁵

5

6 ¹ Department of Earth Sciences, University of Oxford, South Parks Road, Oxford OX1 3AN, UK

7 ² Now at Department of Earth Sciences, University of Cambridge, Downing Street, Cambridge, UK,
8 CB2 3EQ.

9 ³ Washington University in St. Louis, One Brookings Drive, St. Louis, MO 63130

10 ⁴ School of Earth and Environment, Institute of Geophysics & Tectonics, University of Leeds, Leeds
11 LS2 9JT, UK.

12 ⁵ Red Nacional de Vigilancia Volcánica, Servicio Nacional de Geología y Minería, Av. Santa María
13 0104, Providencia, Chile.

14

15 * Corresponding author: pew26@cam.ac.uk. Phone: 07593670818

16 Abstract

17 Previous work has shown that arc volcanics from thick-crustal continental arcs are compositionally
18 distinct from those erupted in island arcs or continental arcs with thinner crust (<30km). However,
19 the relative influence of the slab, mantle, and upper plate on this variability remains poorly
20 constrained. Subduction zones have been the loci of continental crust creation for over 2 Ga, so the
21 processes responsible for this variability have important implications for the chemical evolution of
22 the Earth. The Andean Southern Volcanic Zone (SVZ; 33-46° S) is a particularly suitable setting in
23 which to examine the mechanisms leading to enriched magma compositions in continental arcs,

24 because both crustal thickness and magma chemistry vary consistently along strike. However, the
25 scarcity of primitive samples from the northern SVZ, where the continental crust is thickest (50km),
26 has precluded unbiased comparisons between the southernmost and northernmost volcanoes, and
27 may have contributed to an overemphasis of the role of crustal processing in along-arc trends. This
28 study investigates the geochemistry (major and trace element abundances, $^{87}\text{Sr}/^{86}\text{Sr}$ and
29 $^{143}\text{Nd}/^{144}\text{Nd}$) of new samples from Don Casimiro and Maipo volcanoes, which lie within the
30 Diamante-Maipo Caldera Complex of the northern SVZ. While evolved Diamante-Maipo samples
31 show evidence for crustal assimilation, the trace element and isotopic enrichment of the primitive
32 samples analysed in this study cannot result from crustal processing, because plausible basement
33 lithologies are not uniformly enriched in all of the necessary elements. Recycling of certain crustal
34 lithologies via subduction erosion could potentially generate the isotopic composition of the
35 Diamante-Maipo magmas, but would result in highly irregular trace element patterns that are not
36 observed in the lavas. We argue that the relative enrichment of the northern SVZ is best explained
37 by the presence of an enriched ambient mantle component (similar to EM1-type ocean island
38 basalts), superimposed on a northward decline in melt extent. Rather than crustal recycling, the
39 EM1-like signatures in arc volcanics may arise from recycling of metasomatized subcontinental
40 lithospheric mantle (M-SCLM). This hypothesis is consistent with the isotopic composition of M-
41 SCLM melts across South America, as well as the isotopic compositions of samples from the
42 Argentinian rear arc adjacent to and south of Diamante-Maipo. These rear-arc centres not only
43 corroborate the findings at the arc front, they also demonstrate extensive variability in the supply
44 of slab fluids to regions well behind the arc. Our results caution that if ambient mantle enrichment
45 is not taken into account, petrogenetic models of evolved lavas may exaggerate the role of crustal
46 assimilation, and models for the growth of continental crust may overestimate the amount of
47 continental material that must be recycled back into the mantle to satisfy mass balance.

48

49 Key Words

- 50 • Mantle heterogeneity
- 51 • Andean Southern Volcanic Zone

52 Highlights

- 53 • NSVZ isotopic and trace element enrichment indicate an EM1-like mantle source.
- 54 • EM1-like signatures originate from recycling of M-SCLM from nearby cratons.
- 55 • Slab melting, low mantle melt extents, and M-SCLM may enrich continental arc lavas
- 56 • Slab fluids are not supplied vertically from their point of origin.

57 1. Introduction

58

59 Continental arc magmas, which erupt through thick over-riding crust, are compositionally distinct
60 from oceanic arc magmas. They tend to have elevated incompatible element abundances, steeper
61 incompatible trace element patterns (Fig. 1), and isotopic signatures offset to higher $^{87}\text{Sr}/^{86}\text{Sr}$ and
62 lower $^{143}\text{Nd}/^{144}\text{Nd}$ than oceanic arc magmas (Leeman et al., 1983; Plank and Langmuir, 1988;
63 Hildreth and Moorbath, 1988; Turner et al., 2015a; Farner and Lee, 2017). Many of these
64 compositional characteristics correlate strongly with the thickness of the arc crust (Turner et al.,
65 2015a), and have even been used as proxies to estimate changes in crustal thickness and rates of
66 surface uplift through time (Profeta et al., 2015; Chiaradia, 2015; Chapman et al., 2015; Scott et al.,
67 2018). Much of the compositional offset between thick and thin-crust arcs can be accounted for
68 by higher extents of crystal fractionation and crustal assimilation in continental settings (e.g. Farner
69 and Lee, 2017). However, some compositional differences persist even when considering volcanics
70 that have not been extensively overprinted in the crust (e.g. Plank and Langmuir, 1988; Turner and

71 Langmuir, 2015a; Turner et al., 2017; Schmidt and Jagoutz, 2017), which is suggestive of a mantle
72 origin. Compositional differences among “primary” magmas from continental vs. oceanic settings
73 have been attributed to variations in slab temperature (Ruscitto et al., 2012; Turner and Langmuir,
74 2015b; Schmidt and Jagoutz, 2017), different extents of mantle melting (e.g. Plank and Langmuir,
75 1988; Tormey et al., 1991; Turner et al., 2016), subduction erosion (e.g. Stern, 1989), or mantle
76 heterogeneity that is not the direct result of subducting materials (e.g. Hickey et al., 1986; Ewart
77 and Hawkesworth, 1987; Rogers and Hawkesworth, 1989; Hochstaedter et al., 2001; Pearce et al.,
78 2007; Turner et al., 2017). Our understanding of the thermal structures of subducting plates, the
79 growth of the continental crust, and the petrogenesis of evolved arc magmas depends critically on
80 constraining the relative influence of each of these factors in producing the enriched compositions
81 of continental arc magmas.

82

83 The Andean Southern Volcanic Zone (SVZ) is an excellent natural laboratory in which to investigate
84 how the thick crusts and lithospheres of active compressional plate margins affect the compositions
85 of magmas added to the continents. The SVZ (33-46° S) is one of four volcanically active segments
86 within the Andean Cordillera, where the Nazca Plate subducts under South America. It is commonly
87 subdivided into three segments: the northern, transitional, and southern SVZ (NSVZ, TSVZ and SSVZ
88 respectively; Dungan et al., 2001; Fig. 2a). From the SSVZ to the NSVZ, crustal thickness increases
89 from ~30-50 km (Fig. 2c), slab depth from 70-120 km (Tassara and Echaurren, 2012), the lower
90 plate age from 16-37 Ma (at 42° S and 33° S respectively, Volker et al., 2011), and trench sediment
91 thickness ranges from 1.3-2.1 km (c.f. Hildreth and Moorbath, 1991). There is also a well-
92 established geochemical gradient from the SSVZ to the NSVZ (Tormey et al., 1991; Hildreth and
93 Moorbath, 1988; Hickey et al., 2016, Fig. 2d-e). Trace element abundances of SSVZ volcanoes,
94 where the crust is thinnest, have similar trace element patterns, and fall within the compositional

95 range of island arcs (Fig. 1). The scarcity of primitive lavas from the NSVZ, which overlies the
96 thickest crust, has made it difficult for prior work to assess the chemical characteristics of NSVZ
97 parental magmas, though an average of the more mafic TSVZ lavas (“Central Chile”; Turner and
98 Langmuir, 2015a) indicates substantially higher trace element abundances, which are similar in
99 character to the bulk continental crust and the average of the more mafic volcanics of Cascades
100 stratovolcanoes (Fig. 1). Thus, the chemical variability between the SSVZ and NSVZ are analogous to
101 the chemical offsets between island arcs and continental arcs.

102

103 While many prior studies have addressed the mechanisms producing along-strike compositional
104 variability of the SVZ arc-front volcanoes (Lopez-Escobar et al., 1977; Hickey et al., 1986; Hildreth
105 and Moorbath, 1988; Tormey et al., 1991; Jacques et al., 2014; Hickey et al., 2016), the role of
106 enrichment and heterogeneity within the asthenospheric mantle feeding the arc has received
107 relatively little attention. Such ambient mantle heterogeneity is commonly inferred from trace
108 element and isotopic compositions of mid-oceanic ridge basalts (MORBs) and ocean island basalts
109 (OIBs; Zindler and Hart, 1986; Willbold and Stracke, 2010). In OIBs, this variability can be accounted
110 for by a handful of isotopically distinct end-member components, such as the “enriched mantle”
111 end-members (EM1, EM2; e.g. Zindler and Hart, 1986), which are commonly modelled as the
112 products of recycled lithospheric mantle, sediment, and ancient oceanic/continental crust (c.f.
113 Willbold and Stracke, 2010). There is also evidence for ambient mantle heterogeneity in arcs,
114 despite additional tectonic complexity. For example, a global compilation of samples from rear-arc
115 provinces filtered to minimize slab contributions (Turner and Langmuir, 2015b) form a linear array,
116 extending to EM1-type OIB compositions, which are significantly more isotopically enriched (higher
117 $^{87}\text{Sr}/^{86}\text{Sr}$ and lower $^{143}\text{Nd}/^{144}\text{Nd}$) than the average Depleted MORB Mantle (DMM; Fig. 3a). Models
118 of corner flow find that rear-arc mantle domains are generally transported towards the arc-front.

119 Therefore, this rear-arc data may indicate that ambient sub-arc mantle compositions also vary
120 substantially (e.g. Woodhead et al., 2012). The Andean Southern Volcanic Zone (SVZ) rear arc
121 exemplifies this enriched ambient mantle signature (Kay et al., 2013; Jacques et al. 2013, 2014;
122 Søger et al., 2015a; Turner et al. 2017), with more enriched rear-arc $^{87}\text{Sr}/^{86}\text{Sr}$ and $^{143}\text{Nd}/^{144}\text{Nd}$
123 values than any other arc globally (Fig. 3a). A major goal of this work is thus to assess the relative
124 influence of ambient mantle heterogeneity in a targeted region of the NSVZ.

125

126 This study investigates the petrogenesis of new mafic lava samples from the volcanoes Don
127 Casimiro and Maipo within the Diamante-Maipo Caldera complex (34°S, Fig. 2b), to better
128 determine the geochemical character of NSVZ parental magmas. The lavas from Don Casimiro and
129 the basal portion of Maipo are among the most primitive ever sampled within the NSVZ (Fig. 4a).
130 This may be linked to their eruption immediately after the catastrophic formation (~150ka) of the
131 Diamante Caldera (Orozco et al., 2015), prior to the re-organization and maturation of crustal
132 magma reservoirs. These primitive NSVZ magma compositions allow us to characterise and explore
133 the origins of magmatic enrichment within a thickened continental subduction zone.

134

135 This study also incorporates samples from seven Argentinean monogenetic cones, located up to
136 350 km behind the NSVZ arc front. This rear-arc volcanism initiated in the earliest Miocene,
137 associated with a period of shallow slab subduction (Kay and Copeland, 2006). Steepening of the
138 slab towards the present-day dip of 33° (Tassara and Echarren, 2012) started at 5 Ma (Kay et al.,
139 2005). The samples included in this study are from monogenetic cones that erupted within the last
140 1 Myr, after the cessation of slab steepening. The post-Miocene rear-arc volcanism may be due to
141 the influx of hot asthenosphere during slab steepening from a Middle-Late Miocene flat slab regime
142 (Ramos and Folguera, 2011), possibly in a mantle plume-like configuration (Burd et al., 2014).

143 Regardless of the mode of magmagenesis, these samples provide additional constraints on the
144 composition of the ambient sub-arc mantle beneath the SVZ, and enable examination of slab
145 additions beyond the arc-front.

146

147 2. Samples and methods

148 Of the 15 arc-front samples studied (Fig. 4a-b), six represent the basal sequence of Maipo Volcano,
149 the active stratovolcano at the centre of the Diamante-Maipo Caldera Complex (Fig. 2b). Nine were
150 collected from Don Casimiro Volcano, a small eroded stratovolcano located ~10 km SW of Maipo
151 with activity restricted to preglacial times (Charrier, 1979). $^{40}\text{Ar}/^{39}\text{Ar}$ dates indicate that early
152 activity at these centres was contemporaneous (Orozco et al., 2015). All lavas contain ubiquitous
153 olivine and clinopyroxene phenocrysts within a glassy groundmass. The more evolved samples also
154 contain plagioclase, oxides, and orthopyroxene (details in SIA2). The rear-arc samples are from
155 small monogenetic scoria cones (Fig. 2a). Olivine, clinopyroxene, and oxide phenocrysts dominate,
156 with microcrysts of plagioclase and alkali feldspar, and minor apatite. Whole-rock major-element
157 and trace-element analyses were conducted on all samples, with $^{87}\text{Sr}/^{86}\text{Sr}$ and $^{143}\text{Nd}/^{144}\text{Nd}$ data and
158 olivine major and trace analyses also collected for a subset (methods in SIA3).

159

160 3. Results

161 The new Don Casimiro-Maipo samples are primitive calc-alkaline basaltic andesites to andesites and
162 the rear-arc samples are primitive basalts-trachybasalts (Fig. 4a). Olivine phenocryst compositions
163 range from $\text{Fo}_{75.7}$ - $\text{Fo}_{83.6}$ at the arc-front, and $\text{Fo}_{80.6}$ - $\text{Fo}_{90.1}$ in the rear-arc (Appendix 3; Fig. SB1a). The
164 olivine compositions of the three analysed arc-front samples and most rear-arc samples lie below

165 the olivine – whole rock equilibrium line, indicating that minor olivine accumulation has occurred
166 (up to 7 wt. %; Fig. SB1; Hickey et al., 2016).

167

168 The whole-rock Mg#s of Don Casimiro-Maipo samples mostly range from 60-70, indicating that
169 these samples have undergone only minor crystal fractionation (Fig. 4a). There is little variation in
170 SiO₂ (55.3-57.9 wt.%) within the sample set. Previous studies within the Diamante-Maipo Caldera
171 (Hickey et al., 1986; Futa and Stern, 1988, Sruoga, 2005; Holm et al., 2014) have primarily sampled
172 volcanics with significant europium anomalies ($Eu^* = [Sm_N \times Gd_N]^{0.5}$; Fig. 4b), indicating that samples
173 have undergone fractionation of plagioclase or mixing between primitive and evolved magmas (e.g.
174 Turner and Langmuir, 2015). In contrast, our higher Mg# samples have $Eu/Eu^* > 0.9$ (Fig. 4b).

175

176 Like most arc magmas, the mafic Don Casimiro-Maipo lavas and rear-arc scoria have high
177 abundances of Cs, Rb, Ba, U, Th, Pb, and Sr relative to other elements of similar incompatibility
178 during mantle melting, while Nb and Ta are relatively depleted (Fig. 1). The highly incompatible
179 trace element abundances of the Don Casimiro-Maipo arc-front samples are elevated relative to
180 typical mafic to intermediate samples from oceanic arcs or the SSVZ. Abundances in the rear-arc
181 samples are generally even higher than the arc front. As noted by Holm et al. (2016), the rear-arc
182 samples also have relative depletions in the high field strength elements Zr and Hf. The magnitude
183 of this depletion is on the upper end of what is observed within the SVZ arc front, with $Hf/Sm \sim 0.6$.
184 The Don Casimiro-Maipo samples, however, have smaller relative Zr-Hf depletions than any other
185 primitive samples from the SVZ arc-front, with $Hf/Sm \sim 0.8$ (Fig. SB2). As noted by previous studies
186 (e.g. Hildreth and Moorbath, 1988), Don Casimiro-Maipo and NSVZ samples have lower Cs/Rb than
187 Villarrica and other SSVZ samples.

188

189 Samples from Don Casimiro-Maipo have significantly more enriched isotope ratios (higher $^{87}\text{Sr}/^{86}\text{Sr}$
190 and lower $^{143}\text{Nd}/^{144}\text{Nd}$) than Villarrica and other mafic products from SVZ arc-front centres (Fig. 3b).
191 The isotopic compositions of the most primitive Don Casimiro samples in this study generally have
192 lower $^{87}\text{Sr}/^{86}\text{Sr}$ and higher $^{143}\text{Nd}/^{144}\text{Nd}$ than previously reported samples from the Diamante-Maipo
193 caldera (Fig. 3b). The Maipo samples from this study lie at higher $^{87}\text{Sr}/^{86}\text{Sr}$ and lower $^{143}\text{Nd}/^{144}\text{Nd}$
194 than Don Casimiro Samples. The $^{87}\text{Sr}/^{86}\text{Sr}$ and $^{143}\text{Nd}/^{144}\text{Nd}$ of the rear-arc centres in this study fall
195 between the literature SVZ data and Don Casimiro-Maipo.

196

197 4. Discussion

198 While the gradient of northerly-increasing crustal thickness in the SVZ theoretically provides the
199 ideal setting to understand the relationship between primary magma compositions and crustal
200 thickness, the scarcity of mafic lavas in the NSVZ has made prior assessment of the origin of
201 geochemical variation difficult. The volcanological setting of early Don Casimiro-Maipo lavas
202 allowed the magmas to rapidly ascend through the thick crust of the NSVZ and avoid extensive
203 crystal fractionation. Samples from this unique geological setting can thus be used to improve our
204 understanding of the relative contributions from crustal processing, mantle melting, slab fluxes,
205 subduction erosion, and ambient mantle heterogeneity to the production of compositionally
206 enriched magmas erupted from volcanoes in continental arcs.

207

208 4.1. Crustal processing at Don Casimiro-Maipo

209 When lavas from throughout the Diamante-Maipo caldera complex are considered, there is a clear
210 role for crustal assimilation or mixing during fractional crystallization (AFC). $^{87}\text{Sr}/^{86}\text{Sr}$ and
211 $^{143}\text{Nd}/^{144}\text{Nd}$ values correlate with indices of fractionation (Fig. SB3), and the assimilation of known

212 SVZ basement compositions can recreate the variation in trace element and isotope ratios between
213 the most primitive and most evolved samples (Fig. 4c-d).

214

215 Hildreth and Moorbath (1988) suggested that mantle-derived magmas are processed in a melting,
216 assimilation, storage, and homogenization (MASH) zone in the lower crust. In their model, mantle-
217 derived magmas throughout the SVZ initially have similar compositions, and the enriched
218 “baseline” composition of NSVZ magmas results from increased MASH processing due to the
219 thicker crust. Thus, the isotopic compositions of even the most primitive NSVZ volcanics would be
220 the result of mixing between SSVZ-like mantle melts and some crustal basement component.

221

222 It is not possible to conclusively determine whether the most primitive Don Casimiro-Maipo
223 samples are entirely free of crustal contamination. It is possible, however, to assess the plausibility
224 of a scenario in which the notable compositional differences between the more primitive magmas
225 of the SSVZ and NSVZ are the result of a MASH-like process. Villarrica volcano has a similar trace
226 element and isotopic composition to the other volcanoes of the SSVZ (Fig. 1, Fig. 3b), and has
227 erupted some of the most primitive magmas. For simplicity, an average composition of mafic
228 samples from Villarrica is used to represent the composition of SSVZ volcanics.

229

230 Crustal assimilation and mixing likely affect the evolved magmas of the Diamante Caldera (Sruoga
231 et al., 2005). Mixing between the primitive Don Casimiro-Maipo compositions and a set of sampled
232 crustal lithologies, for example, reproduces the chemical variability observed within the Diamante
233 Caldera (Fig. 4c-d). While it is plausible that the evolved Diamante Caldera lavas can be related to
234 the primitive Don Casimiro-Maipo lavas by a combination of assimilation and fractional
235 crystallization, mixing between these same crustal rocks and primitive Villarrica samples *does not*

236 reproduce the Don Casimiro-Maipo compositions (Fig. 4c-d). These assimilants produce rapidly
237 decreasing K/Rb ratios prior to producing adequate enrichment in $^{87}\text{Sr}/^{86}\text{Sr}$, and none reach high
238 enough Rb/Y. For the MASH model to explain the chemical differences between the NSVZ and SSVZ
239 a lower-crustal assimilant distinct from that producing geochemical variability *within* the Diamante-
240 Maipo caldera must be incorporated into Don Casimiro-Maipo primary magmas.

241

242 To test whether any plausible Andean crustal assimilant may be capable of bridging the
243 compositional gap between Don Casimiro-Maipo and the SSVZ, the compositions of 348 basement
244 outcrops and basement xenoliths from the SVZ and the surrounding area (22-46°S) were compiled
245 (Lucassen et al. 2001; Lucassen et al., 2004 and others; Appendix 5), and mixed with the average
246 composition of primitive Villarrica samples. Only 14% of potential assimilants produce mixed
247 compositions within $^{87}\text{Sr}/^{86}\text{Sr} \pm 0.0001$ and $^{143}\text{Nd}/^{144}\text{Nd} \pm 0.00005$ of the primitive Don Casimiro-
248 Maipo average (Fig. 5a). Of these isotopically plausible mixed compositions, only 35% have Eu
249 anomalies within the range of the primitive Don Casimiro-Maipo samples ($\text{Eu}/\text{Eu}^* > 0.9$). None of
250 these mixed compositions have trace element signatures resembling Don Casimiro-Maipo (Fig. 5b).
251 Incorporating crystal fractionation alongside assimilation cannot account for these compositional
252 offsets, because the resulting compositions produce mismatches not only in overall elemental
253 abundances but also in a variety of incompatible element ratios, and substantial fractional
254 crystallization would rapidly drive down the magmatic Mg#.

255

256 It remains possible that the required MASH assimilant has evaded sampling within the Southern
257 Andes. Consequently, it is worth considering what compositional characteristics a hypothetical
258 assimilant must possess to bridge the compositional gap between the southern and northern SVZ.
259 We assume a maximum of 20% assimilation, based on the relatively high Mg#s of primitive Don

260 Casimiro-Maipo lavas (as assimilation drives cooling, and thus crystal fractionation; DePaolo, 1981).
261 Given this, any suitable assimilant must have greater than ~ 450 ppm Zr, ~ 1420 ppm Sr, and
262 ~ 0.63 wt% P_2O_5 . It is improbable that a crustal rock will possess these characteristics, because these
263 elements typically become depleted, rather than enriched, during late stage crystal fractionation or
264 crustal melting (e.g. Turner and Langmuir, 2015a). To illustrate this point, a compilation of all
265 continental granites, diorites, syenites, and monzonites in the GEOROC database ($N \sim 3000$ with
266 trace element data) was searched for suitable assimilants (considering only trace element
267 abundances). Only 15 samples possessed sufficient concentrations of Zr, Sr, and P_2O_5 . Mixtures of
268 these samples with the average primitive Villarrica composition have erratic trace element
269 patterns, testament to the complex petrological histories of these unusually enriched lithologies.
270 None recreate the observed trace element pattern of Don Casimiro-Maipo, particularly the
271 negative Nb-Ta anomaly (Fig. 5c). Thus, although crustal assimilation is near pervasive among the
272 samples of the NSVZ, and strongly influences the compositions of evolved samples in this region,
273 attributing the compositional offset between the NSVZ and SSVZ to MASH processing is inconsistent
274 with the available data from SVZ basement outcrops, as well as with fundamental considerations
275 regarding the composition of the required assimilant.

276

277 The geochemistry of the northern-most rear-arc samples further reinforces the conclusion that the
278 isotopic offset between NSVZ and SSVZ samples is not a product of MASH. Rear-arc $^{87}Sr/^{86}Sr$ and
279 $^{143}Nd/^{144}Nd$ data fall along the “mantle array” (Fig. 3a; Sørensen et al., 2013; 2015a-b; Sørensen and
280 Holm, 2013; Kay et al., 2013; Jacques et al., 2013; 2014; Holm et al., 2014; Turner et al. 2017),
281 which is difficult to recreate by assimilation of available basement (e.g. Fig. 5a). Additionally, rear-
282 arc isotopic enrichment correlates with arc-front enrichment, despite substantial longitudinal
283 offsets (Fig. 6a-b). This is difficult to reconcile with assimilation, as accretion and eastward

284 migration of the arc-front since the Palaeozoic has produced a longitudinally fragmented basement,
285 with different basement domains striking parallel to the coast (Kay et al., 2005). Assimilation of
286 lithologies within these different basement domains would produce uncorrelated rear-arc and arc-
287 front Sr and Nd isotope systematics and would be unlikely to generate the linear trend on Fig. 3a.
288 Finally, even the most primitive northern rear-arc samples, which bear olivines in equilibrium with
289 their whole-rock compositions and are nearly in equilibrium with the mantle (Fig. SB1), possess
290 enriched trace element and isotopic signatures. It is improbable that such primitive samples have
291 undergone substantial crustal overprinting of $^{87}\text{Sr}/^{86}\text{Sr}$ and $^{143}\text{Nd}/^{144}\text{Nd}$.

292

293 4.2 Assessing the slab and mantle melting contributions to SVZ compositional variation

294 The goal of this section is to determine to what extent slab components and melting processes
295 contribute to the along-strike variability of SVZ volcanics. Volcanic trace-element abundances vary
296 as a function of the extent of mantle melting (F) and residual mantle mineralogy. Highly
297 incompatible elements, which partition preferentially into the melt phase, may have higher
298 concentrations in the NSVZ due to lower F, rather than different mantle source abundances
299 (Tormey et al., 1991). Lower F in the NSVZ may result from the thick northern lithosphere impinging
300 on the mantle wedge (Turner et al., 2016). This would be consistent with the finding of lower F
301 values in volcanic arcs with thicker crust globally (Plank and Langmuir, 1988; Turner and Langmuir,
302 2015b).

303

304 In addition to variability in F, the trace element compositions of primary arc magmas reflect the
305 transportation of slab materials into the mantle wedge. To assess whether the compositions of
306 both Villarrica and Don Casimiro-Maipo can be produced from a common ambient mantle
307 composition with variable slab components and F, it is useful to consider the maximum solution

308 space generated by these parameters alone. For these calculations, we assume slab melting, as the
309 slab top temperatures for Central Chile (784°C, D80 model of Syracuse et al., 2010) lie above the
310 wet pelite and AOC solidi (Hermann and Spandler, 2007; Carter et al. 2015). Furthermore, the
311 Syracuse et al. (2010) D80 values may represent minimum temperatures, given recent evidence for
312 shear heating and shallower depths of slab-mantle coupling (Penniston-Dorland et al., 2015;
313 England, 2018). Slab melt compositions were calculated by mixing the composition of subducted
314 sediment (ODP1232; Turner et al., 2017) and MORB (Gale et al., 2013) in various proportions,
315 following by melting using partition coefficients consistent with experimental values for slab
316 melting at temperatures between 800-900 °C (SIA4.1; Kessel et al., 2005; Hermann and Rubatto,
317 2009; Skora and Blundy, 2010). These slab melts were then mixed with an estimate of the depleted
318 MORB mantle composition (DMM; Workman and Hart, 2005). The composition of mantle melts
319 derived from this mixed composition were calculated using experimentally-derived hydrous
320 partition coefficients and melt reaction coefficients (model details in SIA4.1).

321

322 The resulting solution space is shown in Fig. 7a-b. The red area on Fig. 7a depicts the solutions
323 made available by varying the proportions of slab components and melt extent. $F=0.04$ was chosen
324 as the lowest plausible melt extent because F values <0.04 tend to produce alkali-basalt or silica
325 undersaturated major element compositions (e.g. Baasner et al. 2016). Villarrica samples fall within
326 this solution space (as do most SSVZ samples), and a model fit within this space (purple diamond)
327 reproduces the entire suite of Villarrica incompatible trace elements (Fig. 8). While this model fit
328 does not represent a unique solution for Villarrica, it does demonstrate that a feasible quantitative
329 solution exists that is consistent with available experimental constraints. In contrast, there is no
330 solution for Don Casimiro-Maipo. Increasing the amount of sediment and AOC contributions to the
331 depleted mantle source can recreate the high La/Sm ratios, but only at Sr/Nd values that are far too

332 high (Fig. 7a). While reducing F shifts the melt composition to higher La/Sm, even at $F=0.04$ there is
333 no possible match to the Don Casimiro-Maipo volcanics.

334

335 The composition of the slab components also varies as a function of slab temperature (Hermann
336 and Rubatto, 2009). There are systematic changes in the slab age and depth beneath the SVZ arc
337 front, with corresponding variations in the slab thermal parameter, Φ ($\Phi = \text{slab age} \times \text{convergence}$
338 $\text{rate} \times \sin(\text{dip angle})$). Therefore, one might expect hotter slab temperatures in the NSVZ. However,
339 while the magnitude of geochemical variation in the SVZ comprises much of the compositional
340 range seen among arcs globally, differences in Φ between the SSVZ and NSVZ are relatively minor
341 on the global scale (Turner et al., 2016).

342

343 Certain aspects of the trace element differences between Don Casimiro-Maipo and Villarrica
344 suggest subtle slab temperature variations are indeed present. Compared to Villarrica, Don
345 Casimiro-Maipo has low Cs/Rb and high Hf/Sm (Fig. 1). These element pairs are not substantially
346 fractionated from each other by mantle melting, so likely reflect differences in the mantle source
347 composition. For these element ratios, it is plausible that observed mantle source variations are
348 caused by higher slab temperature in the NSVZ. Cs is highly mobile in low temperature aqueous
349 fluids, and may have been disproportionately lost during early slab dehydration (Savov et al., 2007;
350 Spandler et al., 2007). A hotter slab temperature can also destabilize zircon during slab melting,
351 producing the less pronounced Zr-Hf depletions at Don Casimiro-Maipo (e.g. Hirai et al., 2018). The
352 blue field on Fig. 7a shows the expansion of the available solution space for slab temperatures
353 $>900^\circ\text{C}$, as calculated using the maximum measured experimental mobility of light rare earth
354 elements (LREE) in slab melts. While the solution space shifts toward higher La/Sm at a given Sr/Nd,
355 the mafic NSVZ volcanics still plot well outside of the realm of possible solutions. Despite evidence

356 for differences in SVZ slab temperature, including a slab temperature parameter alongside variable
357 F and varying slab proportions only increases the available solution space to the Red+Blue fields on
358 fig. 7a, which clearly does not envelop the data from Don Casimiro-Maipo.

359

360 The same conclusion can be drawn from $^{87}\text{Sr}/^{86}\text{Sr}$ and $^{143}\text{Nd}/^{144}\text{Nd}$ (Fig. 7b). The isotopic solution
361 space is simplified by the fact that these isotope ratios are not fractionated by melting. The pink
362 field on Fig. 7b shows the solution space produced by variation in slab temperature and the
363 proportions of slab melts. Again, the Don Casimiro-Maipo data falls well outside of the available
364 solution space, because slab contributions predominantly drive wedge compositions to higher
365 $^{87}\text{Sr}/^{86}\text{Sr}$ at near constant or increasing $^{143}\text{Nd}/^{144}\text{Nd}$.

366

367 4.3 Is there geochemical evidence for subduction erosion?

368

369 SVZ rear-arc volcanics form a linear array between MORB-like compositions and EM1-type OIBs in
370 $^{87}\text{Sr}/^{86}\text{Sr}$ vs. $^{143}\text{Nd}/^{144}\text{Nd}$ space (Kay et al., 2013; Søger et al., 2015a; Fig. 3a), and both rear-arc and
371 arc-front samples are characterized by similar along-strike variability in these isotopes (Fig. 6a-b). If
372 the isotopic offset between the mafic NSVZ and SSVZ samples is neither a product of crustal
373 assimilation nor variation in the slab component, some EM1-like contaminant must be introduced
374 to the mantle source of the SVZ. The origins of EM1-type OIBs are debated, with suggestions
375 including deep recycling of lower continental crust (LCC), pelagic sediment and oceanic crust, or
376 metasomatized subcontinental lithospheric mantle (Willbold and Stracke, 2010). The first
377 suggestion is particularly apt in the SVZ, as it has been proposed that the NSVZ endured extensive
378 subduction erosion (the removal of upper plate material via abrasion and plucking by the lower
379 plate) throughout the Cenozoic (Stern, 1989). While the composition of the South Andean LCC is
380 not well constrained, the possible compositions of this reservoir can be inferred from the ever-

381 growing dataset of regional basement compositions (Appendix 5). Although these samples were
382 collected from surface outcrops, such outcrops may be representative of deep crustal lithologies
383 due to Miocene episodes of tectonic thickening and under-thrusting (Hildreth and Moorbath,
384 1991). Thus, this database likely represents lithologies within both the upper and lower crust, and
385 can be used not only to test models of lower crustal recycling, but also recycling of the entire
386 crustal column forming the outbound belt of the South American Plate vulnerable to subduction
387 erosion, including the upper crust (as suggested by Holm et al., 2014; 2016).

388

389 To assess the subduction erosion hypothesis, basement compositions (Appendix 5) were mixed
390 with the estimated composition of the Villarrica mantle source. Only 11% of the mixed
391 compositions pass within $^{87}\text{Sr}/^{86}\text{Sr} \pm 0.0001$ and $^{143}\text{Nd}/^{144}\text{Nd} \pm 0.00005$ of the most primitive Don
392 Casimiro-Maipo samples (Fig. 9a). Only 15% of the isotopically plausible mixed compositions have
393 Eu anomalies within the range of the primitive Don Casimiro-Maipo samples ($\text{Eu}/\text{Eu}^* > 0.9$), none of
394 which recreate the concentrations of Y, Gd, Sm, Sr, Ba and $^{87}\text{Sr}/^{86}\text{Sr}$ ratios (Fig. 9b-c). To conclude,
395 no mixed compositions with adequate trace element data falls within the range of the Don
396 Casimiro-Maipo for $^{87}\text{Sr}/^{86}\text{Sr}$, $^{143}\text{Nd}/^{144}\text{Nd}$, and trace element abundances.

397

398 While some studies in this region (e.g. Holm et al., 2014; 2016) have found that SVZ volcanic
399 compositions can be related by subduction erosion of sampled crustal lithologies, our preceding
400 analysis does not support this conclusion. This is possibly because the newly sampled Don Casimiro-
401 Maipo samples are more primitive, while those in previous studies were affected by plagioclase
402 fractionation, magma mixing, or crustal assimilation, which accounts for their lower Eu/Eu^* values.
403 It is possible that limited basement exposure in the SVZ means that the appropriate mixing lithology
404 has avoided sampling, but regional considerations also indicate the LCC chemical model is

405 implausible. Willbold and Stracke (2010) provide a model by which EM1-like isotopic compositions
406 are produced by mixing LCC starting materials into normal MORB mantle. However, this model
407 assumes that the LCC domains in question have been extracted and isolated from the mantle for >4
408 Ga, while the Chilenia and Cuyania terranes comprising the lower crust of the NSVZ-TSVZ are only
409 of Grenvillian age (~1Ga; Ramos, 2010). Because of this relatively young age, the typical basement
410 of the Southern Andes has $^{143}\text{Nd}/^{144}\text{Nd}$ values that are too high (relative to $^{87}\text{Sr}/^{86}\text{Sr}$) to serve as an
411 appropriate end-member (see mixed compositions in Fig. 9a). When considering the full array of
412 available trace element abundances and isotope values, the subduction erosion hypothesis does
413 not appear to be consistent with the geochemical systematics, possibly indicating that the extent of
414 subduction erosion has been over-estimated for this region. For example, Stern (1989) estimated
415 erosion rates based on the assumption that the distance between the trench and the arc front
416 remained constant throughout the Miocene, while recent geophysical models find that arc-front
417 migration relative to trench location might be a common process (e.g. Karlstrom et al., 2014).
418 Alternatively, subduction erosion may have affected the Andean margin in the past, but the eroded
419 material has since been flushed from the mantle wedge by corner flow.

420

421 Rear-arc geochemical variability is also inconsistent with the subduction erosion hypothesis. Rear-
422 arc isotopic enrichment persists at distances exceeding 600 km from the trench; it seems unlikely
423 that material eroded at the trench could spread hundreds of kilometres in the opposite direction of
424 corner flow. It may instead be carried down with the subducting slab and released alongside other
425 slab inputs, but in this case the enriched signature would co-vary with other slab components.
426 Instead, at 550 km from the trench rear-arc monogenetic samples have Ce/Pb values that range
427 from 5 (similar to the arc front) to >20 (similar to MORBs; Fig. 10b), while rear-arc $^{143}\text{Nd}/^{144}\text{Nd}$
428 ratios are consistently enriched relative to DMM (Fig. 3a). Additionally, within a given latitude

429 bracket rear-arc $^{143}\text{Nd}/^{144}\text{Nd}$ ratios have limited variability, and do not correlate significantly with
430 Ce/Pb or other indices of slab addition. Finally, isotopic enrichment in both the rear arc and arc
431 front increases in a reasonably symmetrical, coherent fashion on either side of a pronounced
432 minima at 39° S (Fig. 6a-b; Turner et al., 2017). Although it has been suggested that subduction
433 erosion increases northwards (Stern, 1989), this phenomenon cannot account for the increase in
434 enrichment south of Villarrica. The spatial systematics of rear-arc compositions are therefore also
435 inconsistent with subduction erosion.

436

437 4.4 EM1-type enrichment from a sub-continental lithospheric mantle source

438 An alternative source for the enriched EM1-like mantle signature of the NSVZ is Metasomatised

439 Subcontinental Lithospheric Mantle (M-SCLM). The infiltration of low degree mantle melts

440 ($F \sim 0.005$) into the base of the lithospheric mantle produces enriched incompatible element

441 concentrations, which rapidly evolve EM1-like isotopic compositions (McKenzie and O’Nions, 1995;

442 Turner et al., 2017; Fig. 11). Additionally, M-SCLM provides a more homogenous end-member

443 composition than crustally-derived materials (Rogers and Hawkesworth, 1989; Turner et al, 2017).

444 This material may be stored for long periods in the lithospheric mantle until it is returned to the

445 asthenosphere by delamination or erosion.

446

447 Field evidence supports the hypothesis that the SCLM surrounding the SVZ has EM1-like isotopic

448 affinities. Three geographically separated suites of isotopically enriched igneous rocks across South

449 America have been interpreted as direct melts of the enriched SCLM (see Fig. 2a):

450 1) Alkaline igneous rocks erupted near the edges of the Rio Apa-Luis Alves and Sao Francisco

451 Cratons (Gibson et al., 1995; 2005; Carlson et al., 1996).

452 2) Mesozoic metabasites from the Southern Rift (Lucassen et al., 2002).

453 3) Carboniferous granitoids from the Santo Domingo Complex of the Coastal Batholith (Parada
454 et al., 1999).

455 The $^{87}\text{Sr}/^{86}\text{Sr}$ and $^{143}\text{Nd}/^{144}\text{Nd}$ of samples from these regions plot as a linear extension of the SVZ
456 rear-arc array (Fig. 11) and cannot be accounted for by addition of variable slab components or
457 assimilation of available basement. The remarkable alignment of these lithologies in isotopic space
458 despite being geographically separated by hundreds to thousands of kilometres suggests that M-
459 SCLM east and north of the SVZ has relatively homogeneous EM1 affinities. The isotopic trajectory
460 of these SCLM melts is consistent with the expected isotopic evolution of SCLM enriched by low
461 degree mantle melts (Turner et al., 2017; Fig. 11). In contrast, the field produced by addition of
462 sampled basement lithologies to the mantle has higher $^{87}\text{Sr}/^{86}\text{Sr}$ at a given $^{143}\text{Nd}/^{144}\text{Nd}$ than the
463 array of SCLM-melts and rear-arc volcanics. Additionally, the isotopic variability induced by
464 basement contamination is significantly broader than the narrow trajectory of rear-arc and M-SCLM
465 melts (grey field, Fig. 11).

466
467 The full trace element pattern of such low-degree, relatively high-pressure mantle melts is difficult
468 to assess, as no appropriate partitioning experiment has been carried out. Instead, a compositional
469 proxy can be calculated by inverting for the mantle source composition of Gough Island EM1-type
470 OIB volcanics (Turner et al., 2017), where enrichment has been linked to deep recycling of SCLM
471 (Gibson et al., 2005). Trace element and isotopic ratios of the inverted source composition were
472 subsequently adjusted within the limits of EM1-like ocean island basalts (Stracke et al. 2003;
473 Willbold and Stracke, 2010) to produce a generic EM1 source (SIA4.2). By including EM1-like mantle
474 heterogeneity as an additional parameter in the forward model, the solution spaces on Fig. 7a-b
475 expands to include the green fields, which finally overlap the primitive Don Casimiro-Maipo trace
476 element concentrations. Furthermore, a model fit was identified that is consistent with the full Don

477 Casimiro-Maipo trace element and isotopic composition (Fig. 7-8). As with the model fit for
478 Villarrica, the Don Casimiro-Maipo model does not represent a unique solution, but is a
479 demonstration of the model's quantitative viability under combined evidence from field and
480 experimental constraints.

481

482 The addition of M-SCLM to the mantle by erosion or delamination at the base of continental
483 cratons behind the volcanic arc also provides a more consistent explanation for the spatial
484 variability of both rear-arc and arc-front SVZ volcanic compositions. Turner et al. (2017) proposed
485 two explanations for the gradual decline in isotopic enrichment towards a distinct minimum at 39°S
486 (Fig. 6a-b). Firstly, they note the presence of a Permian terrane suture at 39° S (Rapalini et al.,
487 2010). It is possible that M-SCLM was lost during rifting or subsequent collision between cratonic
488 blocks (Fig. 12a). Secondly, a slab tear may be present at 200km depth on the lower plate at ~39° S
489 (Pesicek et al., 2012). If M-SCLM is entrained equally throughout the SVZ, upwelling of depleted
490 Pacific mantle (which has not interacted with M-SCLM) through this slab window could dilute the
491 EM1 signature. The upwelling, depleted mantle would then spread northwards and southwards,
492 perhaps aided by toroidal flow around the slab tear (Zandt and Humphreys, 2008), resulting in a
493 gradual northward and southward increase in enrichment (Fig. 12b). This could also potentially
494 explain the magnetotellurically imaged "plume" in the rear-arc (Burd et al., 2014). Geochemical
495 signatures associated with upwelling through a slab window in the Kula Volcanic Field (W. Anatolia,
496 Turkey) are traced over >250km (Klaver et al., 2016), similar to the distances observed here.

497

498 **4.5 The relationship between trace element heterogeneity and mantle mineralogy**
499 If the geochemical differences between the NSVZ and SSVZ serve as an analog for the differences
500 between thin and thick crusted arcs, then ambient mantle enrichment may be a common feature of
501 continental arcs. Determining whether EM1-like signatures within the SVZ are characterized by a

502 distinct mineralogy (peridotite vs. pyroxenite) thus has potential implications for melting reactions
503 within these enriched mantle domains. It has been suggested that SVZ rear-arc EM1 signatures are
504 held within pyroxenitic domains, and that a southward decrease in rear-arc olivine Mn/Fe values
505 results from the presence of pyroxenite source lithologies beneath the southern rear-arc (Søager et
506 al., 2015b; Brandt et al., 2017). However, $^{87}\text{Sr}/^{86}\text{Sr}$ and $^{143}\text{Nd}/^{144}\text{Nd}$ isotopes become *less* EM-1-like
507 as Mn/Fe ratios decrease, which is difficult to reconcile with this interpretation (Fig. 13). Moreover,
508 the samples presented in this study have some of the most enriched isotopic signatures in the rear
509 arc, yet have olivine compositions traditionally associated with a peridotite source (Sobolev et al.,
510 2007; Fig. SB4). This suggests that EM1 isotopic signatures are unrelated, or even anti-correlated to
511 the amount of pyroxenite. Thus, although large pyroxenitic domains may be present in certain
512 areas of the rear arc, the distribution of this material is an unlikely candidate to explain isotopic and
513 trace element trends on the scale of the SVZ as a whole. Crucially, rear-arc isotopic ratios can be
514 reproduced with ~2% addition of the inferred SCLM melts (e.g. Gibson et al. 1995; 2005) to the
515 depleted mantle, which is unlikely to have a detectable influence on erupted olivine phenocryst
516 chemistry. It is also worth considering whether olivine compositional classifications, which have
517 been calibrated primarily for anhydrous ocean island basalts (e.g. Sobolev et al. 2007), can be
518 robustly applied to hydrous systems (Wang et al., 2016). The detailed relationship between erupted
519 olivine compositions and mantle mineralogy in the SVZ, as well as the relationship between mantle
520 mineralogy and general indices of mantle enrichment remains an exciting area of ongoing research.

521

522 4.6 Distribution of the slab components within the mantle

523 The geochemical characteristics of rear-arc centres not only reinforce the conclusions drawn at the
524 arc-front regarding spatial trends in EM1-like enrichment, they also provide novel constraints on
525 the spatial distribution of slab components beyond the arc front. Slab melts have high Th/Nb and

526 Th/La, and low Ce/Pb, so these ratios serve as proxies for the extent to which slab components
527 have infiltrated the mantle source of each monogenetic cone (Johnson and Plank, 1999; Plank,
528 2005). Remarkably, while slab-sensitive ratios generally decline with increasing trench distance,
529 some cones retain elevated Th/La and Th/Nb and low Ce/Pb at nearly 600km from the trench (Fig.
530 10b).

531

532 Highly incompatible trace element ratios of rear-arc samples may also indicate the provenance of
533 rear-arc slab components. Thermal models predict that slab-surface temperatures at SVZ rear-arc
534 depths will be $\sim 250^{\circ}$ C higher than those under the arc front (Syracuse et al., 2010). Such high slab
535 temperatures should lead to a relative reduction of zircon stability in the slab, whereas the rear-arc
536 samples have Zr-Hf anomalies similar to those observed for the SSVZ arc-front (Hirai et al., 2018;
537 Fig. SB2). This indicates that the slab component reaching the rear-arc mantle source may have
538 been extracted from the slab at temperatures similar to the SSVZ arc-front slab component.

539 Significant fractionation of other slab-derived elements would also be expected if slab components
540 were extracted at temperatures $\sim 250^{\circ}$ C higher than at the arc-front. Th/La in slab melts may
541 increase by $\sim 25\%$, and Th/Nb and U/Nb by nearly an order of magnitude (Hermann and Rubatto,
542 2009), which would result in rear-arc and arc-front lavas with distinctly different mixing trajectories
543 for these trace elements. Instead, rear-arc and arc-front samples both lie on mixing lines between
544 the arc-front slab melt composition and a mantle with varying amounts of EM1-like enrichment
545 (Fig. 10a). These observations suggest that very little fractionation of these elements has occurred,
546 which is most simply explained by similar slab top temperatures at the source of arc-front and rear-
547 arc slab inputs.

548

549 The observation that rear-arc mantle sources 600 km from the trench appear to have been
550 infiltrated by a slab component that is similar in composition to the arc-front slab component is
551 surprising. It is conceivable that the rear-arc slab signatures represent remnant metasomatism of
552 the mantle wedge from the period of Miocene shallow subduction. However, the samples of this
553 study were probably erupted between 0.01-0.7 Ma (Folguera et al., 2009), 4-5 million years after
554 the slab began to steepen. As the wedge will have “turned over” ~330km in this time, it is likely that
555 Miocene slab inputs were effectively flushed from the asthenospheric sources of the rear-arc cones
556 of this study. A more plausible explanation for both the abundance and composition of the slab
557 fluxes in the rear-arc is that the slab components added to the sources of subduction volcanics are
558 not derived from the slab directly beneath the sampled cone. Geophysical models demonstrate
559 that mantle flow and compaction pressure gradients can affect the flow paths of materials
560 separated from the slab (e.g. Cagnioncle et al., 2007; Wilson et al., 2014). Thus, the mantle source
561 at the arc front may be influenced by slab components that have been extracted from the slab
562 beyond the arc front, and the rear-arc mantle source may be supplied from small quantities of slab
563 components transported in the opposite direction in regions of low porosity (Cerpa et al., 2017; Fig.
564 14b).

565

566 It also is possible that slab materials could be transported non-vertically by “mélange diapirs”.
567 However, recent experimental work (Cruz-Uribe et al., 2018) found that melts of such diapirs will
568 have likely have >50 wt. % SiO₂, >18 wt. % Al₂O₃, and <8 wt. % MgO, while the most primitive SVZ
569 rear-arc basalts have >10 wt. % MgO, <48 wt. % SiO₂, and <15 wt. % Al₂O₃, as is typical of arc alkali
570 basalts generated by low degrees of melting from a lherzolite source (e.g. Baasner et al., 2016).
571 Additionally, the experimental mélange melts have positive Zr-Hf anomalies while the SVZ rear-arc
572 basalts have negative Zr-Hf anomalies (Fig. 1). We also find the possibility of a mélange diapir

573 ascending far above the slab surface without melting to be fundamentally implausible, given the
574 low wet solidus temperatures of sediments and altered ocean crust (Herman and Rubatto, 2009;
575 Carter et al., 2015). Thus, the geochemical systematics of SVZ rear-arc volcanics appear to be most
576 consistent with a strong role for slab melting followed by advective transport, compaction
577 channelling, down-dragging, and generally non-vertical transport of slab liquids through the mantle
578 wedge, consistent with recent numerical models of two-phase flow in the mantle wedge
579 (Cagnioncle et al., 2007; Wilson et al., 2014; Cerpa et al., 2017).

580

581 4.6 Implications for crustal growth and the thermal structure of the arc crust

582 The extent to which the compositions of continental arc volcanics are inherited from the mantle
583 rather than overprinted in the crust has important implications for models of crustal growth.
584 Abundances of highly incompatible trace elements in oceanic arcs are much lower than those of the
585 bulk continental crust (Fig. 1). If continental growth is driven primarily by the accretion of island
586 arcs, which have incompatible element abundances that are often an order of magnitude lower
587 those estimated for the bulk continental crust (Fig. 1), then the continental crust must represent
588 the result of extreme fractionation or remelting of this arc material, followed by recycling of >90%
589 of the initially emplaced magma back into the mantle. However, continental arc volcanism has also
590 contributed a substantial portion of the bulk material to the continental crust (Cao et al., 2017), and
591 continental arc magmas have trace element patterns that more closely resemble the continents
592 (Fig. 1). If this trace element enrichment is inherited from the mantle, then a substantially smaller
593 amount of material must be returned to the mantle to account for the continental mass balance,
594 possibly closer to 50% (Sisson and Kelemen, 2018). The differences between these two
595 interpretations, in turn, have clear implications for the generation of large-scale mantle
596 heterogeneity.

597

598 Evaluating the role of parental magma enrichment versus crustal overprinting is also critical to
599 understanding the petrogenesis of differentiated arc magmas. If one assumes that an evolved arc
600 magma with an “enriched” isotopic composition originated from a “depleted” mantle source similar
601 to MORB, or that the mantle source has a uniform isotopic composition, they will reasonably infer
602 that the enriched magma is composed largely of recycled crustal material and that isotopic
603 variability among magmas is mostly driven by crustal recycling (e.g. Davidson et al., 1990; Luccasen
604 et al., 2006). If instead one assumes that the mantle source is enriched and heterogeneous, then
605 the inferred proportion of the crustal component in the erupted magma will be smaller. For
606 example if the mantle source is assumed to be isotopically similar to typical MORBs, a mixing
607 exercise such as that shown in Fig. 5 indicates that an average of 40% crustal assimilation is
608 necessary to account for the erupted $^{87}\text{Sr}/^{86}\text{Sr}$ and $^{143}\text{Nd}/^{144}\text{Nd}$ values at Don Casimiro-Maipo.
609 Instead, by invoking an enriched mantle source, we have found that these samples are potentially
610 free of crustal contamination. The magnitude and variability of crustal assimilation and crustal
611 melting have clear implications for our understanding of the thermal structures of volcanic arcs
612 (e.g. Annen and Blundy, 2006).

613

614 5. Conclusions

615 The volcanic products of thick-crustal continental arcs have substantially higher abundances of
616 incompatible trace elements, and more “enriched” isotopic signatures than island arcs. The origin
617 of these enriched signatures has profound implications for the formation of the continental crust
618 and the petrogenesis of evolved magmas. The Andean Southern Volcanic Zone (SVZ) is an ideal
619 natural laboratory for investigating the role of crustal thickness in magma petrogenesis, because

620 along-strike trends in SVZ crustal thickness and magma chemistry are analogous to the salient
621 differences between island arcs and continental arcs. While primitive basaltic lavas are common in
622 the Southern SVZ, mafic magmas are scarce in the Northern SVZ, which has made it difficult to
623 distinguish between crustal and mantle signatures. The trace element and isotopic measurements
624 of new Northern SVZ mafic lava samples from Don Casimiro-Maipo presented in this study provide
625 valuable new constraints on these problems.

626

627 While it has been suggested that the geochemical offset between the northern and southern SVZ is
628 primarily driven by the assimilation of continental crust, the addition of known SVZ basement
629 lithologies to a melt composition characteristic of the Southern SVZ fails to recreate the enriched
630 isotopic and trace element signatures of these new Don Casimiro-Maipo samples. Most mixed
631 compositions have $^{87}\text{Sr}/^{86}\text{Sr}$ values that are too high at a given $^{143}\text{Nd}/^{144}\text{Nd}$, and none have
632 appropriate trace element patterns. Moreover, no plutonic lithology sampled *globally* is sufficiently
633 enriched in the required suite of trace elements, due to the fractionation of accessory phases such
634 as zircon and apatite. Assimilation of these variably enriched lithologies produces erratic trace
635 element patterns, dissimilar to those observed at Don Casimiro-Maipo. Simulating the process of
636 subduction erosion by addition of crustal lithologies to a SSVZ-like mantle source also fails to
637 account for northern enrichment, as the resulting melt compositions display similarly unsuitable
638 isotopic systematics and erratic trace element patterns.

639

640 Variable melt extents arising from the northwards impingement of the upper plate on the mantle
641 wedge likely contribute to the observed trace element variability, but cannot account for the large
642 isotopic differences. Similarly, although trace element and isotopic differences in the slab
643 components of the SSVZ and NSVZ may arise due to differing slab temperatures or proportions of

644 slab components, the solution space made available by these parameters, even in combination,
645 does not encompass the trace element or isotopic compositions of mafic Don-Casimiro Maipo
646 samples.

647

648 Thus, the compositions of primitive Don Casimiro-Maipo lavas appear to require not only the
649 addition of slab melts to the mantle wedge and low degrees of mantle melting, but also an enriched
650 northern SVZ mantle source *prior* to slab metasomatism. This is evident from the fact that no other
651 mechanism can successfully reproduce the compositions of the northern SVZ volcanics.

652 Additionally, rear-arc magmas filtered to only include samples with minimal slab contributions
653 extend along the “mantle array” towards compositions similar to EM1-type OIBs. Finally, the most
654 enriched rear-arc samples lie behind the northern SVZ, with a clear decrease in enrichment
655 southwards towards the SSVZ. A forward model based on an inversion for an EM1-like mantle
656 source can successfully reproduce the isotopic composition and trace element composition of Don-
657 Casimiro Maipo, demonstrating that this interpretation is consistent with available experimental
658 constraints.

659

660 The isotopic trajectory of the rear-arc lavas is co-linear with other South American lavas that are
661 thought to be melts of metasomatized sub-continental lithospheric mantle (M-SCLM). Thus, a
662 plausible origin of the enriched mantle source within the SVZ is the addition of M-SCLM material to
663 the mantle wedge by erosion or delamination from the cratonic lithosphere behind the arc. The
664 presence of significant isotopic enrichment >600km “upstream” of the trench is more consistent
665 with an M-SCLM origin than subduction erosion. While the systematic along and across-arc
666 geochemical variations are difficult to reconcile with assimilation or subduction erosion of
667 regionally variable basement lithologies, the composition of the M-SCLM appears to be relatively

668 homogenous across a large area of South America. Variable mantle enrichment within the SVZ may
669 result from upwelling of depleted mantle through a slab tear or the absence of M-SCLM domains
670 around a paleosuture zone.

671

672 Our new data from the northernmost rear-arc province show that in addition to chemical variability
673 induced by variable M-SCLM addition to the mantle source, some rear-arc cones have highly
674 variable slab inputs that are surprisingly similar in composition to the arc front. This supports recent
675 two-phase flow models indicating non-vertical transport of slab materials (Cagnioncle et al., 2007;
676 Wilson et al., 2014; Cerpa et al., 2017).

677

678 This results of this study imply that the enriched trace element and isotopic compositions of
679 primitive lavas in the thick-crust NSVZ are produced by low degree melting of an enriched
680 ambient mantle that is metasomatized by slab melts, rather than fractionation and crustal
681 assimilation. The similarities between the trace element enrichments of these primitive NSVZ and
682 the bulk continental crust (Fig. 1) suggests that these mantle processes may play a major role in the
683 origin of enriched continental compositions globally. An important avenue of future research is to
684 constrain the extent to which the processes leading to enrichment in the NSVZ are applicable to
685 thick crusted arcs elsewhere. This will require reevaluation of enriched signatures in the most
686 primitive lavas of other thick crusted arcs (e.g. Cascades, Mexico, Guatemala, Colombia). If
687 similarities with the SVZ are found, they will provide valuable constraints on models of continental
688 crust generation and elemental cycling within the silicate earth. For example, if ambient mantle
689 heterogeneity contributes substantially to enriched continental compositions, continental mass
690 balances require smaller amounts of material to be returned to the mantle.

691

692 Acknowledgments

693 The authors acknowledge NERC grant 'Mantle volatiles: processes, reservoirs and fluxes'
694 (NE/M000427/1) for funding, Melissa Murphy for help with clean lab chemistry, Sally Gibson for use
695 of the LA-ICP-MS, Jason Day for helping with analysis, and Patrick Sugden for assistance with
696 sample preparation for Sr and Nd isotopes in Leeds.

697

698

699 Figure Captions

700

701 Fig. 1– Trace element Signatures. Trace elements at Don Casimiro-Maipo (this study) are highly
702 enriched compared with Villarrica and the majority of oceanic arcs, and show slight enrichment
703 over the Cascades and Central Chile (Turner et al., 2016). The trace element pattern is similar to the
704 bulk continental crust (Rudnick and Gao, 2003). Don Casimiro-Maipo shows extreme HREE
705 depletion, indicating abundant garnet in the source mantle. Villarrica shows a very similar trace
706 element signature to other SSVZ centers (Llaima, Puyehue and Osorno are shown here; Turner et al.
707 2016), justifying its use as the SSVZ end-member in the modelling of this study. Rear-arc samples
708 show distinctive arc-like signatures, and even greater enrichment than Don Casimiro-Maipo. Spider
709 diagrams normalized to Pyrolite, McDonough and Sun, (1995).

710

711 Fig. 2-Geographical context and sample locations. a) Map of the SVZ, with segment boundaries
712 defined by Dungan et al. (2001). The location of arc-front volcanoes with primitive samples, and the
713 rear-arc sample locations of this study and the GEOROC database are shown. The locations of
714 inferred M-SCLM melts in Fig. 11 are also shown. Basemap from GEOMAP APP. b) Sample locations

715 of Don Casimiro and Basal Maipo lavas within the Diamante-Maipo Caldera Complex. Imagery from
716 Google Earth. c) Moho depth versus projected latitude within the SVZ. Moho depth is calculated at
717 each volcanic centre south of Don Casimiro-Maipo in a) from Tassara and Echaurren (2012).
718 Projected latitude is calculated by projecting a GPS co-ordinate along the convergence vector of the
719 Nazca plate to the Chile trench (Turner et al., 2017). d) and e) Major and trace element
720 concentrations in primitive samples (Turner et al. 2016 and this study) increase northwards,
721 mirroring changes in crustal thickness.

722

723 Fig. 3- Isotopic and trace element variability within the Andean SVZ placed within a global context.

724 a) Literature SVZ rear-arc samples filtered to remove high slab inputs ($\text{Th}/\text{Nb} < 0.4$) fall on a mantle
725 array between DMM and EM1-type ocean island basalts, greatly extending the variability observed
726 globally in rear-arc provinces (rear-arc averages from Turner et al., 2017). Fields are drawn
727 incorporating EM1 and EM2-type ocean island basalts from Stracke et al. (2003). Literature values
728 from Don Casimiro-Maipo lie at the enriched end of this field with respect to global rear-arc
729 variability. The isotopic end-members used for modelling are shown. The EM1 model isotopic
730 composition is taken from a sample from Pitcairn (57DS9; Stracke et al., 2003), which falls near the
731 enriched end of EM1-type ocean island basalts. The depleted end member, Baseline Andean
732 Mantle (BAM), was chosen to plot at the depleted end of the rear-arc array (Sample 126171 from
733 Sjøager et al., 2013). The Nazca Plate sediment composition is calculated from ODP1232 (Turner et
734 al., 2017). b) Don Casimiro and Maipo samples from this study show significantly more enriched
735 isotopic compositions than other SVZ arc-front centres (Turner et al., 2016). Villarrica lies at the
736 depleted end of the SVZ arc-front array. Within the Diamante-Maipo caldera, more evolved
737 samples from Don Casimiro and Maipo plot alongside literature data, following a shallower
738 trajectory than that separating Don Casimiro and Villarrica.

739

740 Fig. 4-Sample Characteristics. a) Don Casimiro-Maipo samples from this study are primitive basaltic
741 andesites. These samples significantly extend the number of primitive analyses available for this
742 centre. Circled samples are believed to have undergone olivine addition (Fig. SB1). Rear-arc samples
743 are primitive basalts-trachybasalts. b) Eu anomalies are negligible in the most primitive samples of
744 this study (>0.9), whereas the majority of literature samples show substantial anomalies. Eu/Eu^*
745 was calculated with $\text{Eu}^* = (\text{Sm}_N \times \text{Gd}_N)^{0.5}$ or with $\text{Eu}^{**} = (\text{Sm}^2 \times \text{Tb})^{1/3}$ where no Gd data was reported.
746 In both cases, element concentrations are normalized to CI chondrite (McDonough and Sun, 1995).
747 c-d) Assimilation of eight SVZ basement sample into primitive Don Casimiro-Maipo samples
748 produce mixing lines that encompass the isotopic and trace element chemical diversity within the
749 Diamante Caldera (from Lucassen et al. 2001; 84-31-1, 84-31-2, 84-42-1, 84-42-11, and Lucassen et
750 al. 2004; 00-77, 00-55, 00-58 and 00-05; lithologies chosen as they best recreate the variability
751 within the Diamante-Maipo caldera). However, assimilation of the same 8 samples cannot recreate
752 the separation between Don Casimiro-Maipo and Villarrica (grey lines). Models originate from the
753 primitive average of Don Casimiro-Maipo and Villarrica samples. Error bars in c) show $\pm 1\sigma$ of the
754 variation among primitive samples.

755

756 Fig. 5-Testing crustal assimilation models. a) Isotopic mixing lines produced by assimilation of 348
757 crustal lithologies thought to be representative of SVZ basement (compiled from GEOROC and
758 other sources) into the average composition of primitive Villarrica samples. Only a small proportion
759 pass near Don Casimiro-Maipo. b) Trace element patterns of the mixed compositions that produce
760 isotopic ratios close to Don Casimiro-Maipo (red lines in a), and have $\text{Eu}/\text{Eu}^* > 0.9$. c) Mixed
761 compositions for the small subset of the ~ 3000 plutonic rocks from GEOROC that have sufficient
762 concentrations of Zr, Sr and P_2O_5 to recreate the enrichment of these elements at Don Casimiro-

763 Maipo. Mixed compositions were calculated for the % mixing required to recreate Zr
764 concentrations. All produce erratic trace element patterns, with none recreating the distinctive Nb-
765 Ta enrichment at Don Casimiro-Maipo.

766

767 Fig. 6 - Across and along-arc variation in rear-arc isotopes. a-b) Rear-arc isotopic ratios form
768 latitudinally coherent trends, with statistically significant R^2 values ($p < 0.005$). A pronounced
769 minimum in $^{87}\text{Sr}/^{86}\text{Sr}$, and a maximum in $^{143}\text{Nd}/^{144}\text{Nd}$ is observed at $\sim 39^\circ \text{S}$, with a reasonably linear
770 and symmetric decrease to the north and south. Rear-arc samples from this study fit within the
771 regional trends. Arc-front centres lie close to the rear-arc best fit line, showing that these spatial
772 trends in enrichment are also present at the arc-front. The deviation in $^{143}\text{Nd}/^{144}\text{Nd}$ between the
773 rear-arc and the arc-front south of 39°S likely results from the sparse sampling of rear-arc centres,
774 making it difficult to resolve regional trends from local variations in heterogeneity. This difference
775 may also reflect much smaller slab input to the rear-arc than arc-front

776

777 Fig. 7 – Trace element and isotopic solution space produced by varying the composition of slab
778 melts, the extent of melting, and the composition of the ambient mantle. a) The red field
779 represents the maximum solution space available by the addition of varying slab melt compositions
780 (up to 2% sediment melt, 10% AOC melt) to a depleted mantle (“baseline ambient mantle” (BAM),
781 with a trace element composition of DMM, and isotopic composition of Sample 126171; Søger et
782 al., 2013) melted at $F=0.04-0.3$. The blue field represents the additional solution space made
783 available by an increase in slab temperature (with a change in the partition coefficients of La, Sm,
784 and Nd; see SIA4.1). The green field represents the additional solution space made available by
785 mixing in various proportions of an EM1-like mantle source to BAM. b) The pink field represents the
786 solution space made available by varying the proportion of AOC and sediment, and the total

787 amount of slab melt, as well as slab temperature. The latter has a much smaller effect than in a),
788 hence the red and blue fields are combined for simplicity. As in a), the green field shows the
789 additional solution space made available by increasing enrichment. In both figures, it is clear that
790 only increasing EM1-like enrichment can recreate the composition at Don Casimiro-Maipo. The
791 diamonds represent the best model fits for Villarrica (F=0.1, 7.5% slab addition consisting of 17%
792 sediment, with no enrichment) and Don Casimiro-Maipo (F=0.056, 7.5% slab addition consisting of
793 23% sediment, with 80% EM1 enrichment). The full trace element signatures of these models are
794 shown in Fig. 8.

795

796 Fig. 8 – Trace element modelling results. The trace element composition of Villarrica can be well
797 matched at F=0.1 with addition of 7.5% slab melt consisting of 17% sediment. The extreme trace
798 element enrichment at Don Casimiro-Maipo is best recreated by addition of 80% enriched source,
799 and slight changes in the composition of the slab addition (23% AOC vs. 17% at Villarrica). The solid
800 black lines in both figures represents the best model fit for each centre at the enrichment and
801 proportions of AOC:SED mentioned above using low temperature slab partition coefficients. This
802 provides the best match for Villarrica. The dashed grey lines represent the model fit for each centre
803 at increased slab temperatures, assuming 70% loss of Cs in the forearc. This provides the best
804 model match for Don Casimiro-Maipo. Model envelopes are produced by adding and subtracting 1σ
805 of 33 measurements of ODP1232 (Turner et al., 2017). Melting conditions generated directly from
806 the physical modelling results of Turner et al. (2016).

807

808 Fig. 9– Modelling contamination of the mantle source by subduction erosion. a) Isotope systematics
809 of contamination of the Villarrica mantle source by subduction erosion. The isotopic composition of
810 the Villarrica mantle source was calculated from the Villarrica primitive average. Only a small

811 percentage of mixing lines pass near Don Casimiro-Maipo. b-c) Trace element and isotopic
812 signatures of the mixed compositions that produce isotopic ratios close to Don Casimiro-Maipo (red
813 lines in a), and have $Eu/Eu^* > 0.9$. The trace element composition of the Villarrica mantle source
814 was calculated from the best model fit in Fig. 8. None of these lithologies can recreate Sr, Ba and
815 $^{87}Sr/^{86}Sr$ systematics at Don Casimiro-Maipo. Error bars show 1σ of primitive samples at Don
816 Casimiro-Maipo and Villarrica based on 5 and 3 analyses respectively.

817

818 Fig. 10- Variation in rear-arc slab inputs. a) Mixing models of slab-sensitive ratios between a melt of
819 a rear-arc mantle source ($F=0.02$, melting at 3.3Gpa) that has not received slab inputs, and a melt of
820 a rear-arc mantle source at the same conditions that has received slab inputs (20% sediment, 80%
821 AOC). The orange wedge reflects progressive mixing of 10% slab (with $ODP1232 \pm 1\sigma$) into a mantle
822 source with 0% EM1 enrichment, and the green wedge reflects mixing of 17% slab (with $ODP1232 \pm$
823 1σ) into a mantle source with 80% EM1 enrichment. Rear-arc trace element ratios follow these
824 mixing lines remarkably closely, with the small amount of scatter likely explained by variable
825 conditions of melting along the rear-arc. b) Trace element ratios sensitive to slab additions versus
826 trench distance. MORB-OIB like values (red bar) start to appear at distances greater than 425km.
827 Remarkably high, arc-like ratios are seen up to 600km from the trench, with large scatter in ratios
828 at large trench distances, contrary to the narrow range of observed isotopes.

829

830 Fig. 11 –Isotopic compositions of inferred SCLM melts within South America (approximate locations
831 on Fig. 2a). These clearly extend the array that passes from DMM/DAM through the arc-front and
832 rear-arc, to Don Casimiro-Maipo. The field produced by contaminating the Villarrica mantle source
833 with crustal lithologies (Fig. 9a) is also overlain. This follows a much shallower trajectory than SCLM
834 melts, and is significantly broader than the SCLM field. Mobile belt M-SCLM melts represent

835 alkaline volcanics erupted on the edges of the Sao Fransisco craton and the Rio Apa-Luis Alves
836 craton on the east coast of South America (Gibson et al., 1995; 2005 and Carlson et al., 1996).
837 Southern Rift melts were erupted just north of the NSVZ (Lucassen et al., 2002). Carboniferous
838 granitoids are from the Santo Domingo Complex of the Coastal Batholith (Parada et al., 1999). All
839 are suggested to have sampled M-SCLM. The green and blue lines show a recycling model in which
840 low degree melts are extracted from the depleted mantle (Salters and Stracke, 2004) and then aged
841 for up to 2 Ga using the parameters from Stracke et al. (2003; c.f. Turner et al., 2017). A model with
842 $F=0.003-0.008$ encapsulates the range of isotopic compositions observed in SCLM melts.

843

844 Fig. 12- Schematic diagrams showing possible explanations for the isotopic enrichment minimum,
845 and its relationship to tectonic features. a) A Permian suture zone corresponds with an absence of
846 M-SCLM. b) A slab tear allows depleted Pacific MORB mantle to upwell, and dilute the EM1-type
847 enrichment above the tear. As the proportion of depleted Pacific MORB mantle declines
848 northwards and southwards, isotopic signatures become more enriched. Upper plate geometry
849 adapted from box model of Sjøager et al. (2015b), pp. 1514.

850

851 Fig. 13 – Assessing olivine chemistry alongside regional isotopic trends. Olivine Mn/Fe decreases
852 southwards. However, over the same interval, there is a decrease in isotopic enrichment
853 southwards. Literature values from Brandt et al. (2017), with rear-arc olivine compositions of this
854 study overlain.

855

856 Fig. 14 – Schematic diagrams of rear-arc slab supply. a) Traditional model of slab supply, with
857 buoyant rise of slab fluids to the rear-arc from a slab melting at higher pressure and temperature
858 than at the arc-front. The composition of these fluids should change with increasing trench

859 distance, as the depth to the slab increases. Additionally, at large trench distances, very little to no
860 slab supply would be expected, due to the exhaustion of hydrous phases. b) Proposed model of this
861 study, inspired by Cagniole et al. (2007), Wilson et al. (2014) and Cerpa et al. (2017). Down
862 dragging of fluids released at arc-front depths explains the similar composition of arc-front and
863 rear-arc slab supply.

864 References

865 Annen, C., Blundy, J.D. and Sparks, R.S.J., 2006. The genesis of intermediate and silicic magmas
866 in deep crustal hot zones. *Journal of Petrology*, **47(3)**, pp. 505-539.

867

868 Baasner, A., Médard, E., Laporte, D. and Hoffer, G., 2016. Partial melting of garnet lherzolite
869 with water and carbon dioxide at 3 GPa using a new melt extraction technique:
870 implications for intraplate magmatism. *Contributions to Mineralogy and
871 Petrology*, **171(5)**, p.45.

872

873

874 Brandt, F.E., Holm, P.M. and Søger, N., 2017. South-to-north pyroxenite–peridotite source
875 variation correlated with an OIB-type to arc-type enrichment of magmas from the
876 Payenia backarc of the Andean Southern Volcanic Zone (SVZ). *Contributions to
877 Mineralogy and Petrology*, **172(1)**, pp. 1-25.

878

879 Burd, A.I., Booker, J.R., Mackie, R., Favetto, A. and Pomposiello, M.C., 2014. Three-dimensional
880 electrical conductivity in the mantle beneath the Payun Matru volcanic field in the
881 Andean backarc of Argentina near 36.5° S: evidence for decapitation of a mantle plume

882 by resurgent upper mantle shear during slab steepening. *Geophysical Journal*
883 *International*, **198**, pp. 812–827.

884
885 Cagnioncle, A.M., E. Parmentier, and L. T. Elkins-Tanton., 2007. Effect of solid flow above a
886 subducting slab on water distribution and melting at convergent plate boundaries.
887 *Journal of Geophysical Research*, **112 (B9)**.

888
889 Cao, W., Lee, C.T.A. and Lackey, J.S., 2017. Episodic nature of continental arc activity since 750
890 Ma: A global compilation. *Earth and Planetary Science Letters*, **461**, pp.85-95.

891
892 Carlson, R.W., Esperanca, S. and Svisero, D.P., 1996. Chemical and Os isotopic study of
893 Cretaceous potassic rocks from southern Brazil. *Contributions to Mineralogy and*
894 *Petrology*, **125(4)**, pp.393-405.

895
896 Carter, L.B., Skora, S., Blundy, J.D., De Hoog, J.C.M. and Elliott, T., 2015. An experimental study
897 of trace element fluxes from subducted oceanic crust. *Journal of Petrology*, **56(8)**,
898 pp.1585-1606.

899
900 Cerpa, N.G., Wada, I. and Wilson, C., 2017. Fluid migration in the mantle wedge: Influence of
901 mineral grain size and mantle compaction. *Journal of Geophysical Research: Solid Earth*,
902 **122**, doi:10.1002/2017JB014046.

903

904 Chapman, J.B., Ducea, M.N., DeCelles, P.G. and Profeta, L., 2015. Tracking changes in crustal
905 thickness during orogenic evolution with Sr/Y: An example from the North American
906 Cordillera. *Geology*, **43(10)**, pp.919-922.

907

908

909 Charrier, R., 1979. Los Volcanes Andres y Don Casimiro: Dos centros descubiertos en los Andes
910 entre 34° S Y 34° S 45' Latitud Sur. *Revista Geologica de Chile*, **8**, pp. 79–85.

911

912 Chiaradia, M., 2015. Crustal thickness control on Sr/Y signatures of recent arc magmas: an
913 Earth scale perspective. *Scientific reports*, **5**, p.8115.

914

915 Cruz-Uribe, A.M., Marschall, H.R., Gaetani, G.A. and Le Roux, V., 2018. Generation of alkaline
916 magmas in subduction zones by partial melting of mélange diapirs—An experimental
917 study. *Geology*, **46(4)**, pp.343-346.

918

919 Davidson, J.P., McMillan, N.J., Moorbath, S., Wörner, G., Harmon, R.S. and Lopez-Escobar, L.,
920 1990. The Nevados de Payachata volcanic region (18 S/69 W, N. Chile) II. Evidence for
921 widespread crustal involvement in Andean magmatism. *Contributions to Mineralogy
922 and Petrology*, **105(4)**, pp.412-432.

923

924 DePaolo, D.J., 1981. Trace element and isotopic effects of combined wallrock assimilation and
925 fractional crystallization. *Earth and Planetary Science Letters*, **53(2)**, pp.189-202.

926

927 Dungan, M.A., Wulff, A. and Thompson, R., 2001. Eruptive stratigraphy of the Tatara–San
928 Pedro complex, 36 S, Southern Volcanic Zone, Chilean Andes: reconstruction method
929 and implications for magma evolution at long-lived arc volcanic centers. *Journal of*
930 *Petrology*, **42(3)**, pp.555-626.

931

932 England, P., 2018. On shear stresses, temperatures, and the maximum magnitudes of
933 earthquakes at convergent plate boundaries. *Journal of Geophysical Research: Solid*
934 *Earth*.

935

936 Ewart, A. and Hawkesworth, C.J., 1987. The Pleistocene-Recent Tonga-Kermadec arc lavas:
937 interpretation of new isotopic and rare earth data in terms of a depleted mantle source
938 model. *Journal of Petrology*, **28(3)**, pp.495-530.

939

940 Farner, M.J. and Lee, C.T.A., 2017. Effects of crustal thickness on magmatic differentiation in
941 subduction zone volcanism: A global study. *Earth and Planetary Science Letters*, **470**,
942 pp.96-107.

943

944 Folguera, A., Naranjo, J.A., Orihashi, Y., Sumino, H., Nagao, K., Polanco, E. and Ramos, V.A.,
945 2009. Retroarc volcanism in the northern San Rafael Block (34–35 30 S), southern
946 Central Andes: Occurrence, age, and tectonic setting. *Journal of Volcanology and*
947 *Geothermal Research*, **186(3)**, pp. 169-185.

948

949 Futa, K. and Stern, C.R., 1988. Sr and Nd isotopic and trace element compositions of
950 Quaternary volcanic centers of the southern Andes. *Earth and Planetary Science*
951 *Letters*, **88(3-4)**, pp.253-262.

952

953 Gale, A., Dalton, C. A., Langmuir, C. H., Su, Y. and Schilling, J. G., 2013. The Mean Composition
954 of Ocean Ridge Basalts. *Geochemistry, Geophysics, Geosystems*, **14(3)**, pp. 489–518.

955

956 Gibson, S. A., Thompson, R. N., Day, J. A., Humphris, S. E. and Dickin, A. P., 2005. Melt-
957 generation processes associated with the Tristan mantle plume: Constraints on the
958 origin of EM-1. *Earth and Planetary Science Letters*, **237(3-4)**, pp. 744–767.

959

960 Gibson, S. A., Thompson, R. N., Leonardos, O. H., Dickin, A. P., Mitchell, J. G., Paranaíba, A. and
961 Province, I., 1995. The Late Cretaceous Impact of the Trindade Mantle Plume : Evidence
962 from Magmatism in SE Brazil. *Journal of Petrology*, **36 (1)**, pp. 189-229.

963

964 Hermann, J. and Rubatto, D., 2009. Accessory phase control on the trace element signature of
965 sediment melts in subduction zones. *Chemical Geology*, **265(3-4)**, pp. 512–526.

966

967 Hermann, J. and Spandler, C.J., 2007. Sediment melts at sub-arc depths: an experimental
968 study. *Journal of Petrology*, **49(4)**, pp.717-740.

969

970 Hickey, R.L., Frey, F.A., Gerlach, D.C. and Lopez-Escobar, L., 1986. Multiple sources for basaltic
971 arc rocks from the southern volcanic zone of the Andes (34–41 S): trace element and

972 isotopic evidence for contributions from subducted oceanic crust, mantle, and
973 continental crust. *Journal of Geophysical Research: Solid Earth*, **91(B6)**, pp.5963-5983.
974

975 Hickey-Vargas, R., Holbik, S., Tormey, D., Frey, F.A. and Roa, H.M., 2016. Basaltic rocks from the
976 Andean Southern Volcanic Zone: Insights from the comparison of along-strike and
977 small-scale geochemical variations and their sources. *Lithos*, **258**, pp.115-132.
978

979 Hildreth, W. and Moorbath, S., 1988. Crustal contribution to arc magmatism in the Andes of
980 Central Chile. *Contributions to Mineralogy and Petrology*, **98**, pp. 455–489.
981

982 Hildreth, W. and Moorbath, S., 1991. Reply to Comment on “Crustal contributions to arc
983 magmatism in the Andes of Central Chile” by W. Hildreth and S. Moorbath.
984 *Contributions to Mineralogy and Petrology*, **108(1)**, pp. 247-252.
985

986 Hirai, Y., Yoshida, T., Okamura, S., Tamura, Y., Sakamoto, I. and Shinjo, R., 2018. Breakdown of
987 residual zircon in the Izu arc subducting slab during backarc rifting. *Geology*, **46(4)**,
988 pp.371-374.
989

990 Hochstaedter, A., Gill, J., Peters, R., Broughton, P., Holden, P. and Taylor, B., 2001. Across-arc
991 geochemical trends in the Izu-Bonin arc: Contributions from the subducting slab.
992 *Geochemistry, Geophysics, Geosystems*, **2(7)**, 2000GC000105.
993

994 Holm, P.M., Sjøger, N., Alfatsen, M. and Bertotto, G.W., 2016. Subduction zone mantle
995 enrichment by fluids and Zr–Hf-depleted crustal melts as indicated by backarc basalts of
996 the Southern Volcanic Zone, Argentina. *Lithos*, **262**, pp. 135-152.
997

998 Holm, P.M., Sjøger, N., Dyhr, C.T. and Nielsen, M.R., 2014. Enrichments of the mantle sources
999 beneath the Southern Volcanic Zone (Andes) by fluids and melts derived from abraded
1000 upper continental crust. *Contributions to Mineralogy and Petrology*, **167(5)**, p.1004.
1001

1002 Jacques, G., Hoernle, K., Gill, J., Hauff, F., Wehrmann, H., Garbe-Schönberg, D., van den
1003 Bogaard, P., Bindeman, I. and Lara, L. E., 2013. Across-arc geochemical variations in the
1004 Southern Volcanic Zone, Chile (34.5-38.0° S): Constraints on mantle wedge and slab
1005 input compositions. *Geochimica et Cosmochimica Acta*, **123**, pp. 218–243.
1006

1007 Jacques, G., Hoernle, K., Gill, J., Wehrmann, H., Bindeman, I. and Lara, L. E., 2014. Geochemical
1008 variations in the Central Southern Volcanic Zone, Chile (38 – 43 ° S): The role of fluids
1009 in generating arc magmas. *Chemical Geology*, **371**, pp. 27–45.
1010

1011 Johnson, M. C., and Plank, T., 1999. Dehydration and melting experiments constrain the fate of
1012 subducted sediments. *Geochemistry, Geophysics, Geosystems*, **1(1)**, 1007,
1013 doi:10.1029/1999GC000014.
1014

1015 Karlstrom, L., Lee, C.T. and Manga, M., 2014. The role of magmatically driven lithospheric
1016 thickening on arc front migration. *Geochemistry, Geophysics, Geosystems*, **15(6)**,
1017 pp.2655-2675.

1018

1019 Kay, S.M. and Copeland, P., 2006. Early to middle Miocene backarc magmas of the Neuquén
1020 Basin: Geochemical consequences of slab shallowing and the westward drift of South
1021 America. *Geological Society of America Special Papers*, **407(9)**, pp. 185–213.

1022

1023 Kay, S.M., Godoy, E. and Kurtz, A., 2005. Episodic arc migration, crustal thickening, subduction
1024 erosion, and magmatism in the south-central Andes. *Bulletin of the Geological Society
1025 of America*, **117(1–2)**, pp. 67–88.

1026

1027 Kay, S.M., Jones, H.A. and Kay, R.W., 2013. Origin of Tertiary to Recent EM1 and subduction-
1028 like chemical and isotopic signatures in Auca Mahuida region (37-38S) and other
1029 Patagonian plateau lavas. *Contributions to Mineralogy and Petrology*, **166(1)**, pp. 165–
1030 192.

1031

1032 Kessel, R., Schmidt, M.W., Ulmer, P. and Pettke, T., 2005. Trace element signature of
1033 subduction-zone fluids, melts and supercritical liquids at 120–180 km
1034 depth. *Nature*, **437(7059)**, p.724.

1035

1036 Klaver, M., Davies, G.R. and Vroon, P.Z., 2016. Subslab mantle of African provenance
1037 infiltrating the Aegean mantle wedge. *Geology*, **44(5)**, pp. 367-370.

1038

1039 Leeman, W.P., 1983. The influence of crustal structure on compositions of subduction-related
1040 magmas. *Journal of Volcanology and Geothermal Research*, **18(1-4)**, pp.561-588.

1041

1042

1043 Lopez-Escobar, L., Frey, F.A. and Vergara, M., 1977. Andesites and high-alumina basalts from
1044 the central-south Chile High Andes: geochemical evidence bearing on their
1045 petrogenesis. *Contributions to Mineralogy and Petrology*, **63(3)**, pp.199-228.

1046

1047 Lucassen, F., Becchio, R., Harmon, R., Kasemann, S., Franz, G., Trumbull, R., Wilke, H., Romer,
1048 R. L. and Dulski, P., 2001. Composition and density model of the continental crust at an
1049 active continental margin — the Central Andes between 21 ° S and 27 ° S.
1050 *Tectonophysics*, **341(1)**, pp. 195–223.

1051

1052 Lucassen, F., Escayola, Æ. M., Romer, A. R. L., Kerstin, V. Æ. and Gerhard, K. Æ., 2002. Isotopic
1053 composition of Late Mesozoic basic and ultrabasic rocks from the Andes (23 – 32 ° S) –
1054 implications for the Andean mantle. *Contributions to Mineralogy and Petrology*, **143(3)**
1055 pp. 336–349.

1056

1057 Lucassen, F., Kramer, W., Bartsch, V., Wilke, H.G., Franz, G., Romer, R.L. and Dulski, P., 2006.
1058 Nd, Pb, and Sr isotope composition of juvenile magmatism in the Mesozoic large
1059 magmatic province of northern Chile (18–27 S): indications for a uniform subarc
1060 mantle. *Contributions to Mineralogy and Petrology*, **152(5)**, p.571.

1061

1062 Lucassen, F., Trumbull, R., Franz, G., Creixell, C., Vásquez, P., Romer, R. L. and Figueroa, O.,
1063 2004. Distinguishing crustal recycling and juvenile additions at active continental
1064 margins: The Paleozoic to recent compositional evolution of the Chilean Pacific margin
1065 (36-41° S). *Journal of South American Earth Sciences*, **17(2)**, pp. 103–119.

1066

1067 McDonough, W.F. and Sun, S.S., 1995. The composition of the Earth. *Chemical Geology*, **120**,
1068 pp. 223-253.

1069

1070 McKenzie, D.A.N. and O'Nions, R.K., 1995. The source regions of ocean island basalts. *Journal*
1071 *of Petrology*, **36(1)**, pp.133-159.

1072

1073 Orozco, G., Garces, F., Jara, G., and Lara, L.E., 2015. Nuevos antecedentes para la geología del
1074 complejo volcánico Maipo-Diamante, Andes del Sur. Congreso Geologico Chileno, La
1075 Serena, Octubre 2015. (abstract – accessed
1076 http://biblioteca.sernageomin.cl/opac/DataFiles/14905_v3_pp_218_221.pdf, 13th
1077 January, 2018).

1078

1079 Parada, M.A., Nyström, J.O. and Levi, B., 1999. Multiple sources for the Coastal Batholith of
1080 central Chile (31–34 S): geochemical and Sr–Nd isotopic evidence and tectonic
1081 implications. *Lithos*, **46(3)**, pp.505-521.

1082

1083 Pearce, J.A., Kempton, P.D. and Gill, J.B., 2007. Hf–Nd evidence for the origin and distribution
1084 of mantle domains in the SW Pacific. *Earth and Planetary Science Letters*, **260(1)**, pp.98-
1085 114.

1086

1087 Penniston-Dorland, S.C., Kohn, M.J. and Manning, C.E., 2015. The global range of subduction
1088 zone thermal structures from exhumed blueschists and eclogites: Rocks are hotter than
1089 models. *Earth and Planetary Science Letters*, **428**, pp.243-254.

1090

1091 Pesicek, J. D., Engdahl, E. R., Thurber, C. H., Deshon, H. R. and Lange, D., 2012. Mantle
1092 subducting slab structure in the region of the 2010 M8.8 Maule earthquake (30-40° S),
1093 Chile. *Geophysical Journal International*, **191(1)**, pp. 317–324.

1094

1095 Plank, T. and Langmuir, C.H., 1988. An evaluation of the global variations in the major element
1096 chemistry of arc basalts. *Earth and Planetary Science Letters*, **90**, pp. 349–370.

1097

1098 Plank, T., 2005. Constraints from thorium/lanthanum on sediment recycling at subduction
1099 zones and the evolution of the continents. *Journal of Petrology*, **46(5)**, pp.921-944.

1100

1101 Profeta, L., Ducea, M.N., Chapman, J.B., Paterson, S.R., Gonzales, S.M.H., Kirsch, M., Petrescu,
1102 L. and DeCelles, P.G., 2015. Quantifying crustal thickness over time in magmatic arcs.
1103 *Scientific Reports*, **5**, p.17786.

1104

1105 Ramos, V.A., 2010. The Grenville-age basement of the Andes, *Journal of South American Earth*
1106 *Sciences*, **29**, pp. 77–91.

1107

1108 Ramos, V.A. and Folguera, A., 2011. Payenia volcanic province in the Southern Andes: An
1109 appraisal of an exceptional Quaternary tectonic setting. *Journal of Volcanology and*
1110 *Geothermal Research*, **201(1–4)**, pp. 53–64.

1111

1112 Rapalini, A.E., de Luchi, M.G.L., Dopico, C.M., Klinger, F.G.L., Giménez, M.E., Martínez, P., 2010.
1113 Did Patagonia collide with Gondwana in the Late Paleozoic? Some insights from a

1114 multidisciplinary study of magmatic units of the North Patagonian Massif. *Geologica*
1115 *Acta*, **8**, 349-371.

1116

1117 Rogers, G. and Hawkesworth, C.J., 1989. A geochemical traverse across the North Chilean
1118 Andes: evidence for crust generation from the mantle wedge. *Earth and Planetary*
1119 *Science Letters*, **91**, pp. 271-285.

1120

1121 Rudnick, R.L. and Gao, S., 2003. Composition of the continental crust. In: *Treatise on*
1122 *Geochemistry: The Crust* (Eds. R. Rudnick), **vol. 3**. Permagon, New York, pp. 1–64.

1123

1124 Ruscitto, D.M., Wallace, P.J., Cooper, L.B. and Plank, T., 2012. Global variations in H₂O/Ce: 2.
1125 Relationships to arc magma geochemistry and volatile fluxes. *Geochemistry,*
1126 *Geophysics, Geosystems*, **13(3)**.

1127

1128 Salters, V.J. and Stracke, A., 2004. Composition of the depleted mantle. *Geochemistry,*
1129 *Geophysics, Geosystems*, **5(5)**.

1130

1131 Savov, I.P., Ryan, J.G., D'Antonio, M. and Fryer, P., 2007. Shallow slab fluid release across and
1132 along the Mariana arc-basin system: Insights from geochemistry of serpentinized
1133 peridotites from the Mariana fore arc. *Journal of Geophysical Research: Solid*
1134 *Earth*, **112(B9)**.

1135

1136 Schmidt, M.W. and Jagoutz, O., 2017. The global systematics of primitive arc melts.
1137 *Geochemistry, Geophysics, Geosystems*, **18(8)**, pp.2817-2854.

1138

1139 Scott, E.M., Allen, M.B., Macpherson, C.G., McCaffrey, K.J., Davidson, J.P., Saville, C. and Ducea,
1140 M.N., 2018. Andean surface uplift constrained by radiogenic isotopes of arc
1141 lavas. *Nature Communications*, **9(1)**, p.969.

1142

1143 Sisson, T.W. and Kelemen, P.B., 2018. Near-solidus melts of MORB+ 4 wt% H₂O at 0.8–2.8
1144 GPa applied to issues of subduction magmatism and continent formation. *Contributions*
1145 *to Mineralogy and Petrology*, **173(9)**, p.70.

1146

1147 Skora, S. and Blundy, J., 2010. High-pressure hydrous phase relations of radiolarian clay and
1148 implications for the involvement of subducted sediment in arc magmatism. *Journal of*
1149 *Petrology*, **51(11)**, pp.2211-2243.

1150

1151 Søger, N. and Holm, P.M., 2013. Melt-peridotite reactions in upwelling eclogite bodies:
1152 Constraints from EM1-type alkaline basalts in Payenia, Argentina. *Chemical Geology*,
1153 **360–361**, pp. 204–219.

1154

1155 Søger, N., Holm, P.M. and Llambías, E.J., 2013. Payenia volcanic province, southern mendoza,
1156 argentina: OIB mantle upwelling in a backarc environment. *Chemical Geology*, **349–350**,
1157 pp. 36–53.

1158

1159 Søger, N., Martin, P. and Thirlwall, M.F., 2015a. Lithos Sr , Nd , Pb and Hf isotopic constraints
1160 on mantle sources and crustal contaminants in the Payenia volcanic province,
1161 Argentina. *Lithos*, **212–215**, pp. 368–378.

1162

1163 Søger, N., Portnyagin, M., Hoernle, K., Holm, P. M., Hauff, F. and Garbe-Schanberg, D., 2015b.

1164 Olivine major and trace element compositions in Southern Payenia Basalts, Argentina:

1165 Evidence for pyroxenite-peridotite melt mixing in a back-arc setting. *Journal of*

1166 *Petrology*, **56(8)**, pp. 1495–1518.

1167

1168 Sobolev, A. V., Hofmann, A. W., Kuzmin, D. V., Yaxley, G. M., Arndt, N. A., Chung, S.-L.,

1169 Danyushevsky, L. V., Elliott, T., Frey, F. A., Garcia, M. O., Gurenko, A. A., Kamenetsky, V.

1170 S., Kerr, A. C., Krivolutsкая, N. A., Matvienkov, V. V., Nikogosian, I. K., Rocholl, A.,

1171 Sigurdsson, I. A., Sushchevskaya, N. M. and Teklay, M., 2007. The amount of recycled

1172 crust in sources of mantle derived melts. *Science*, **316**, pp. 412–417.

1173

1174 Spandler, C., Mavrogenes, J. and Hermann, J., 2007. Experimental constraints on element

1175 mobility from subducted sediments using high-P synthetic fluid/melt inclusions.

1176 *Chemical Geology*, **239(3)**, pp.228-249.

1177

1178 Sruoga, P., Llambías, E.J., Fauqué, L., Schonwandt, D. and Repol, D.G., 2005. Volcanological and

1179 geochemical evolution of the Diamante Caldera–Maipo volcano complex in the

1180 southern Andes of Argentina (34 10 S). *Journal of South American Earth Sciences*, **19(4)**,

1181 pp.399-414.

1182

1183 Stern, C.R., 1989. Pliocene to present migration of the volcanic front, Andean Southern

1184 Volcanic Zone. *Andean Geology*, **16(2)**, pp.145-162.

1185

1186 Stracke, A., Bizimis, M. and Salters, V.J., 2003. Recycling oceanic crust: Quantitative
1187 constraints. *Geochemistry, Geophysics, Geosystems*, **4(3)**.

1188
1189 Syracuse, E. M., van Keken, P. E., Abers, G. A., Suetsugu, D., Bina, C., Inoue, T., Wiens, D. and
1190 Jellinek, M., 2010. The global range of subduction zone thermal models, *Physics of the*
1191 *Earth and Planetary Interiors*, **183(1–2)**, pp. 73–90.

1192
1193 Tassara, A. and Echaurren, A., 2012. Anatomy of the Andean subduction zone: Three-
1194 dimensional density model upgraded and compared against global-scale models.
1195 *Geophysical Journal International*, **189(1)**, pp. 161–168.

1196
1197 Tormey, D., Hickey-Vargas, R., Frey, F., Lopez-Escobar, L., 1991. Recent lavas from the Andean
1198 front (32 to 42° S); Interpretations of along-arc compositional variations. *Geological*
1199 *Society of America, Special Paper*, **265**, pp. 57–77.

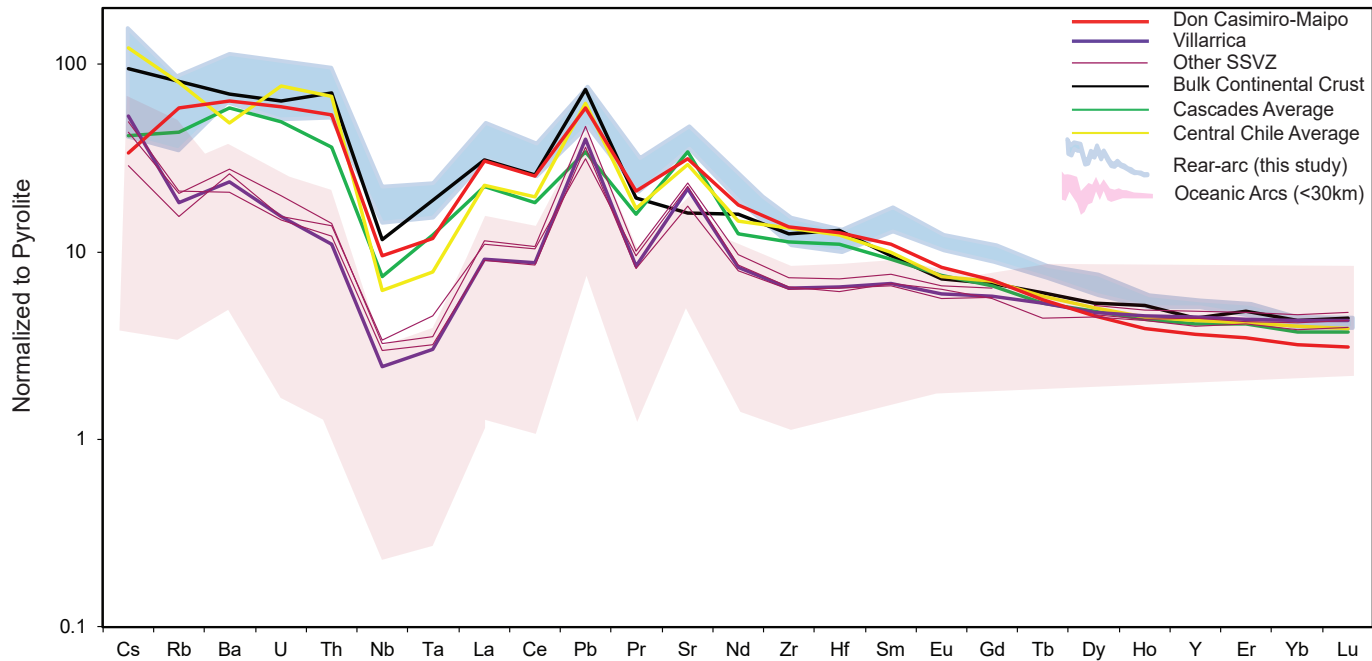
1200
1201 Turner, S.J. and Langmuir, C.H., 2015a. The global chemical systematics of arc front
1202 stratovolcanoes: Evaluating the role of crustal processes. *Earth and Planetary Science*
1203 *Letters*, **422**, pp.182-193.

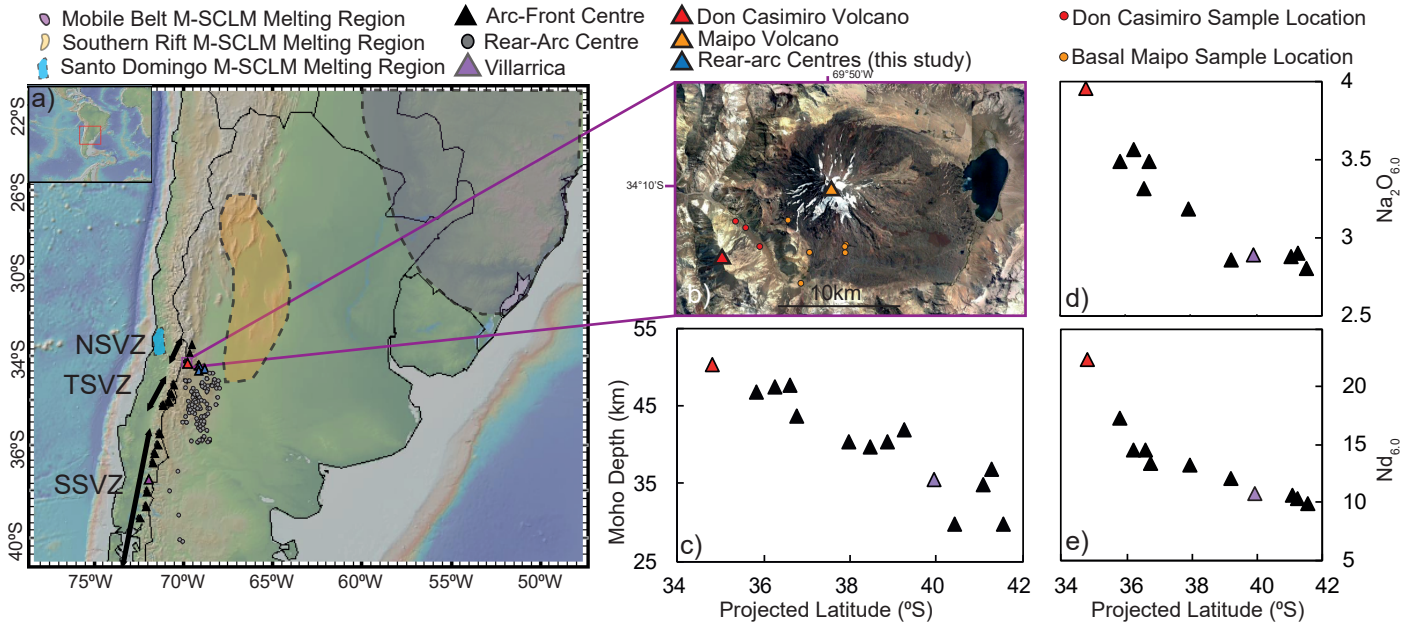
1204
1205 Turner, S. J., and Langmuir, C. H., 2015b, What processes control the chemical compositions of
1206 arc front stratovolcanoes? *Geochemistry, Geophysics, Geosystems*, **16**, pp. 1865–1893.

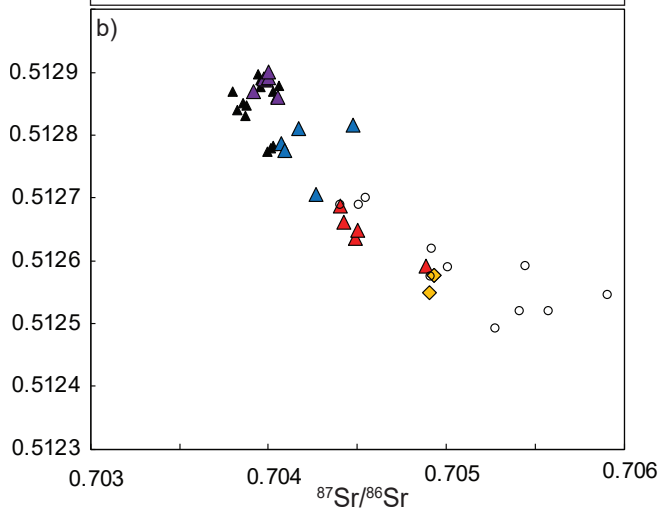
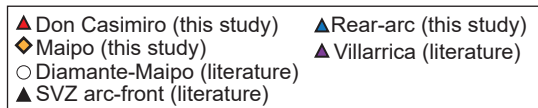
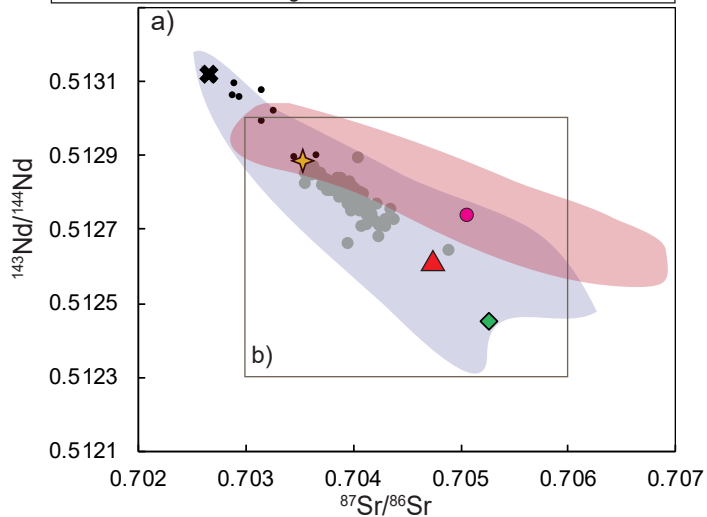
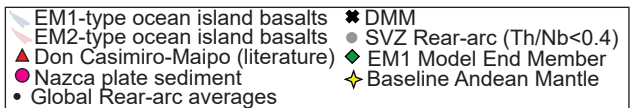
1207

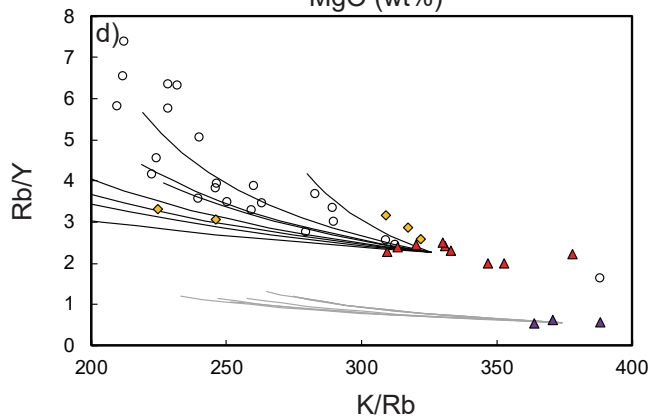
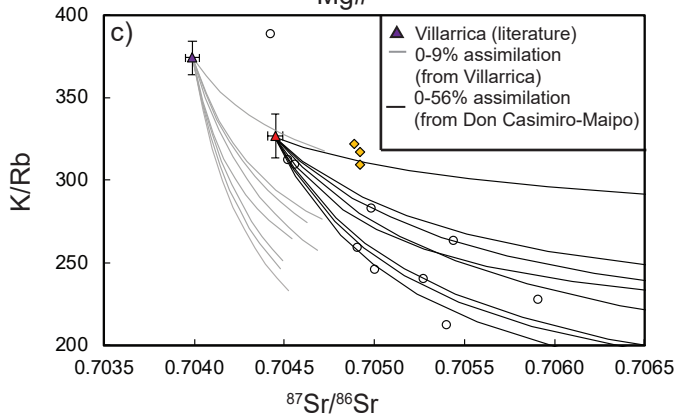
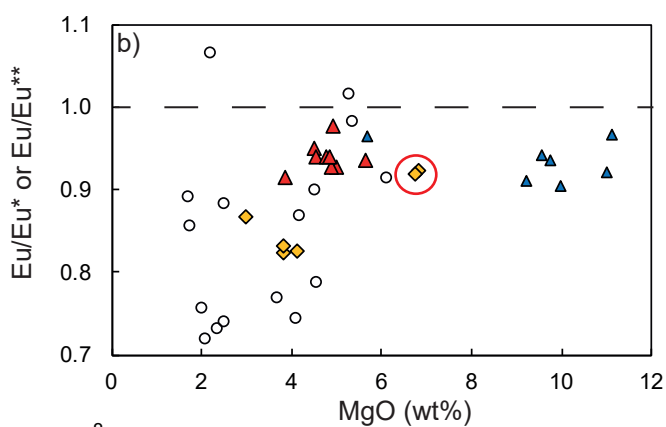
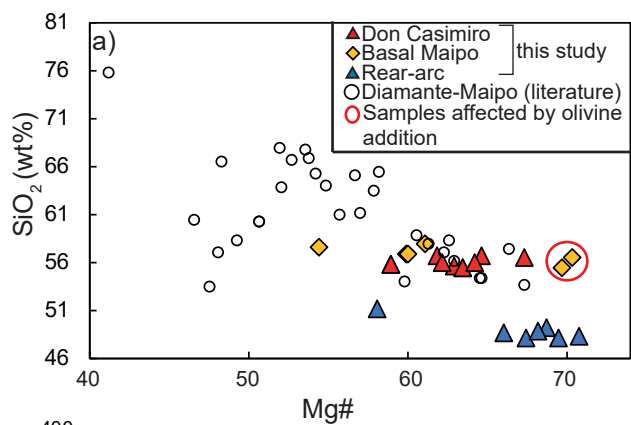
1208 Turner, S. J., Langmuir, C. H., Katz, R. F., Dungan, M. A. and Escrig, S., 2016. Parental arc magma
1209 compositions dominantly controlled by mantle-wedge thermal structure. *Nature*
1210 *Geoscience*, **9**, pp. 772-776,
1211
1212 Turner, S.J., Langmuir, C.H., Dungan, M.A. and Escrig, S., 2017. The importance of mantle
1213 wedge heterogeneity to subduction zone magmatism and the origin of EM1. *Earth and*
1214 *Planetary Science Letters*, **472**, pp.216-228.
1215
1216 Völker, D., Kutterolf, S. and Wehrmann, H., 2011. Comparative mass balance of volcanic
1217 edifices at the southern volcanic zone of the Andes between 33 S and 46 S. *Journal of*
1218 *Volcanology and Geothermal Research*, **205(3-4)**, pp.114-129.
1219
1220 Wang, J., Li, L., Xiong, X., 2016. Trace Element Partitioning during Hydrous Mantle Melting and
1221 Source Mineralogy of Arc Basalts. *Goldschmidt Conference Abstracts*, **3322**.
1222
1223 Willbold, M. and Stracke, A. 2010. Formation of enriched mantle components by recycling of
1224 upper and lower continental crust. *Chemical Geology*, **276(3-4)**, pp. 188-197.
1225
1226 Wilson, C.R., Spiegelman, M., van Keken, P.E. and Hacker, B.R., 2014. Fluid flow in subduction
1227 zones: the role of solid rheology and compaction pressure. *Earth and Planetary Science*
1228 *Letters*, **401**, pp. 261-274.
1229

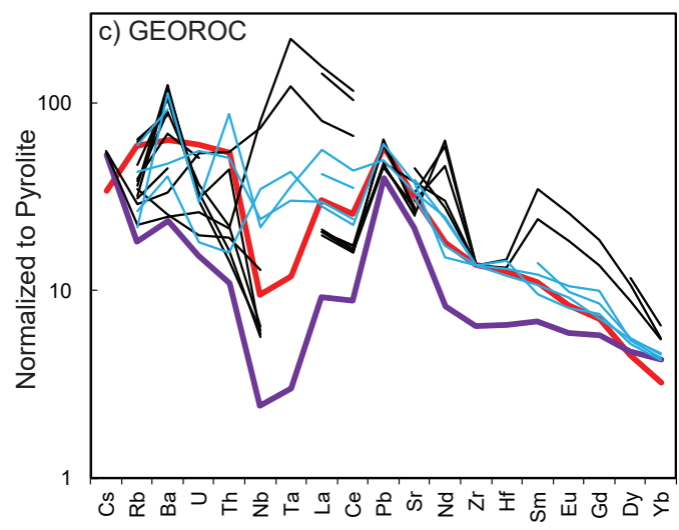
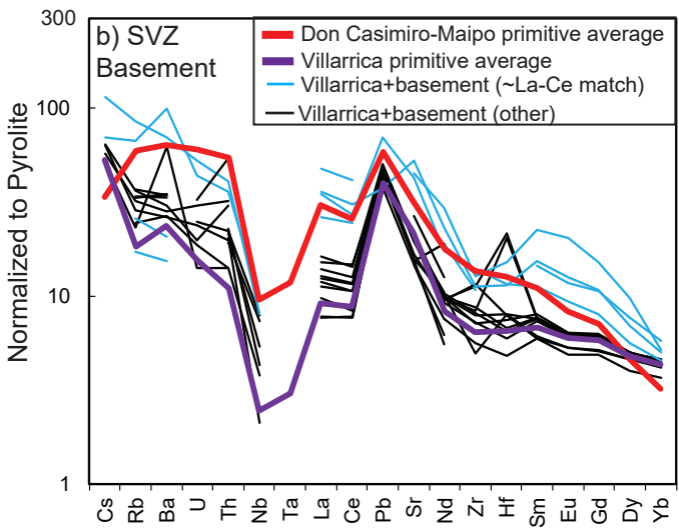
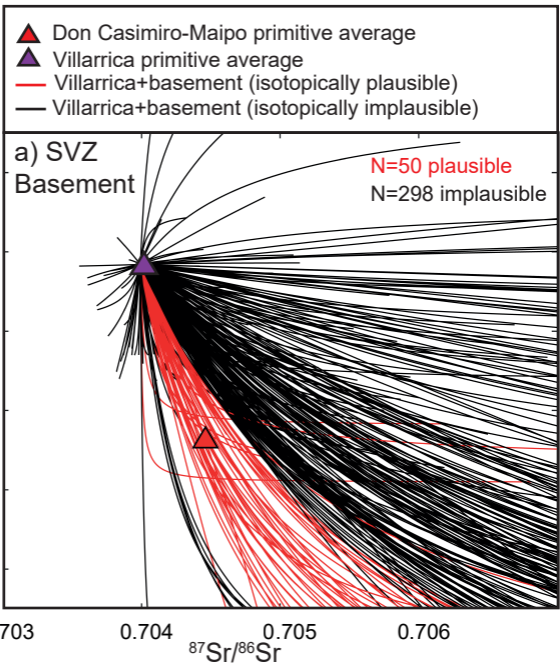
1230 Woodhead, J., Stern, R.J., Pearce, J., Hergt, J., Vervoort, J., 2012. Hf-Nd isotope variation in
1231 Mariana Trough basalts: The importance of “ambient mantle” in the interpretation of
1232 subduction zone magmas. *Geology*, **40**, pp. 539-542
1233
1234 Workman, R.K. and Hart, S.R., 2005. Major and trace element composition of the depleted
1235 MORB mantle (DMM). *Earth and Planetary Science Letters*, **231(1–2)**, pp. 53–72.
1236
1237 Zandt, G. and Humphreys, E., 2008. Toroidal mantle flow around the western US slab window.
1238 *Geology*, **36(4)**, pp. 295-298.
1239
1240 Zindler A., and Hart S., 1986. Chemical Geodynamics. *Annual Review of Earth Planetary*
1241 *Sciences*, **14**, pp. 493–571
1242

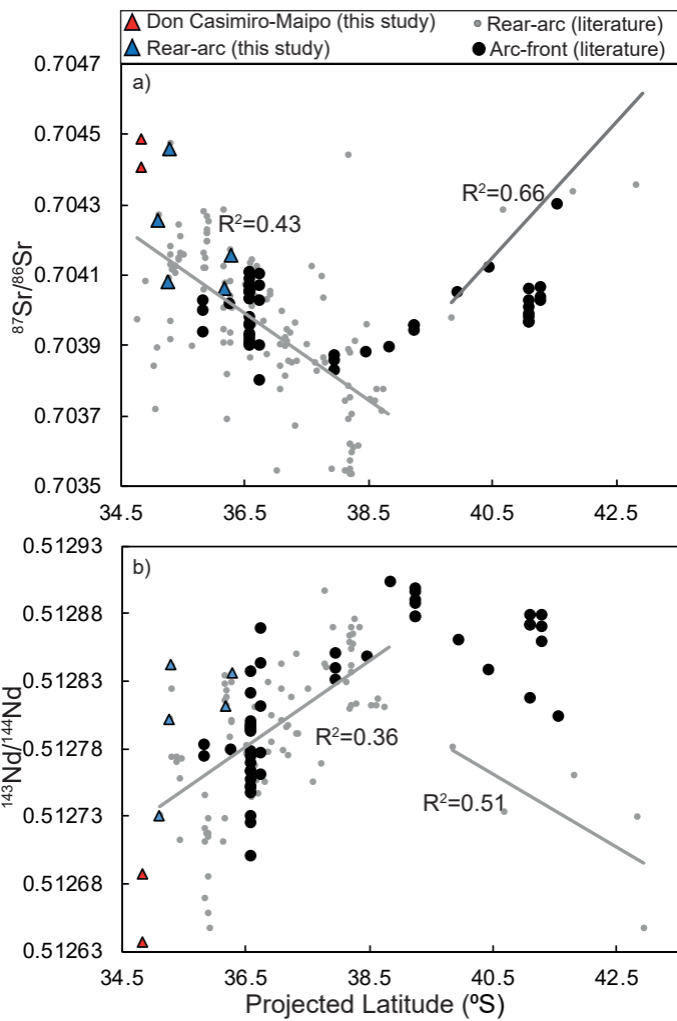


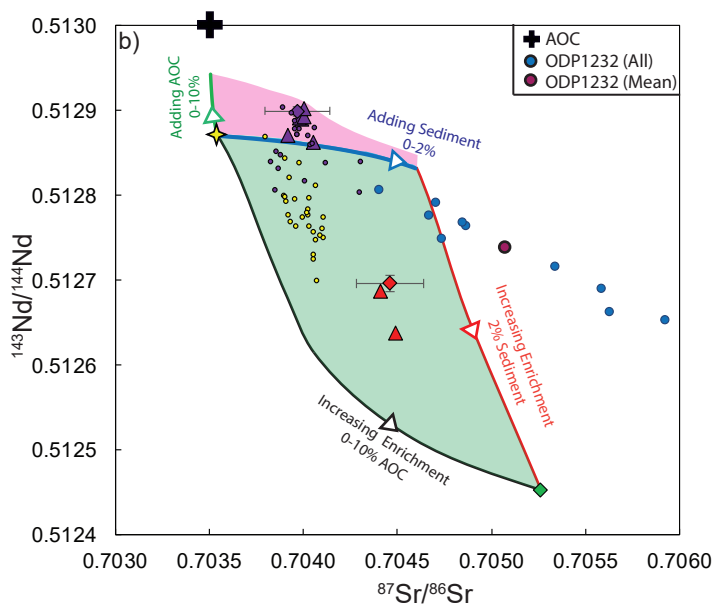
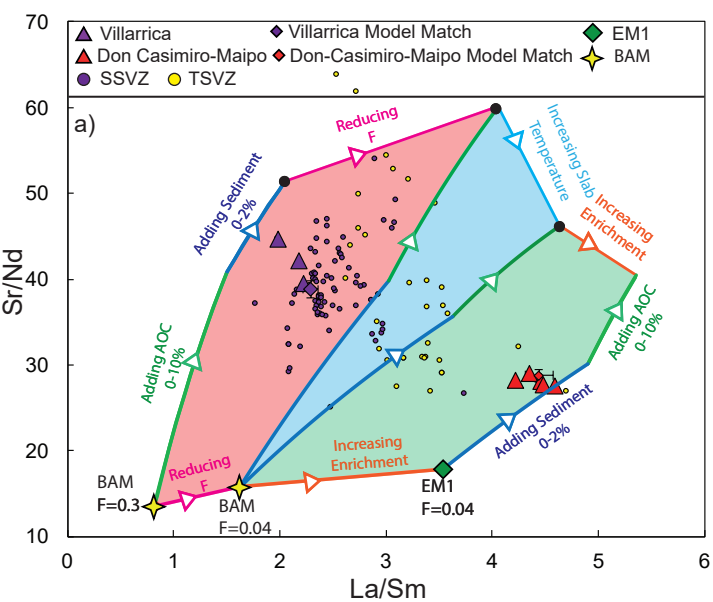




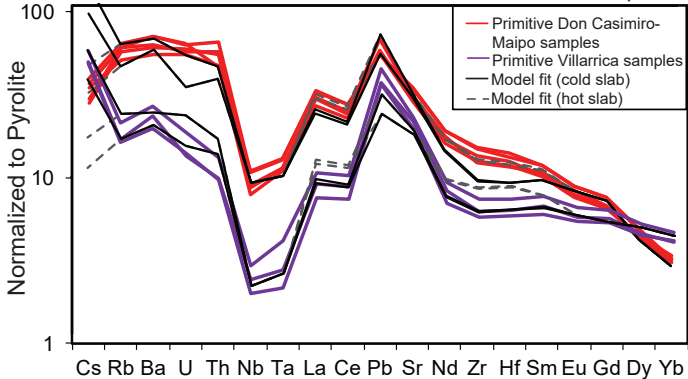




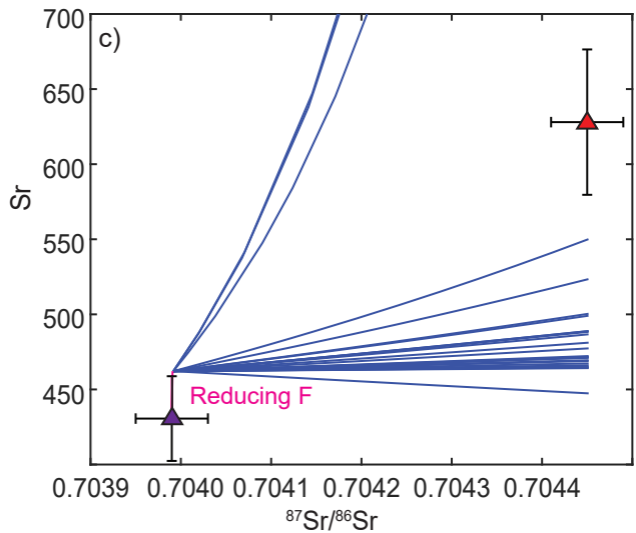
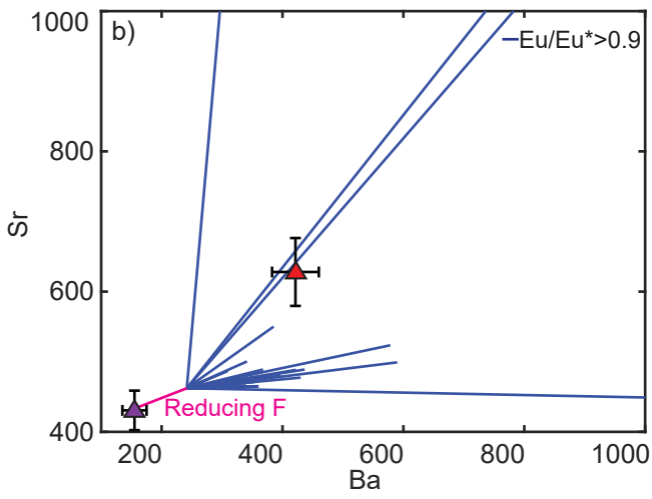
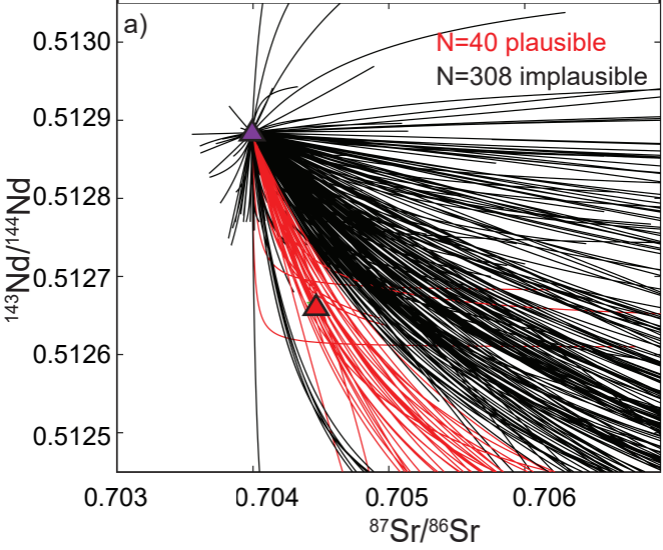


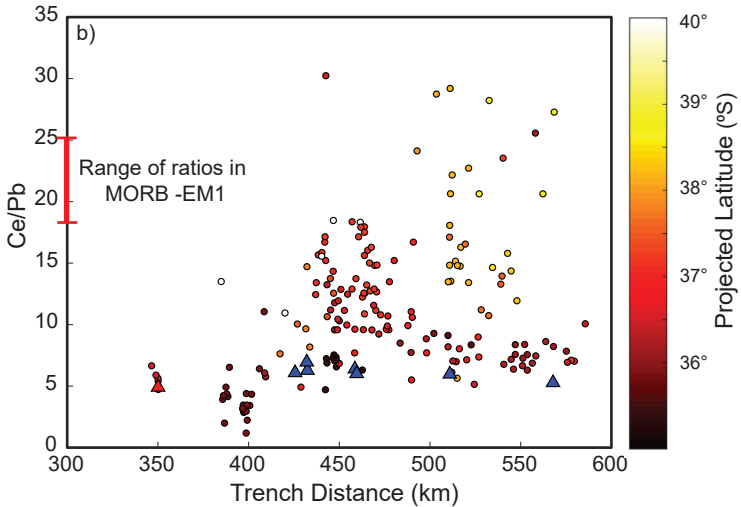
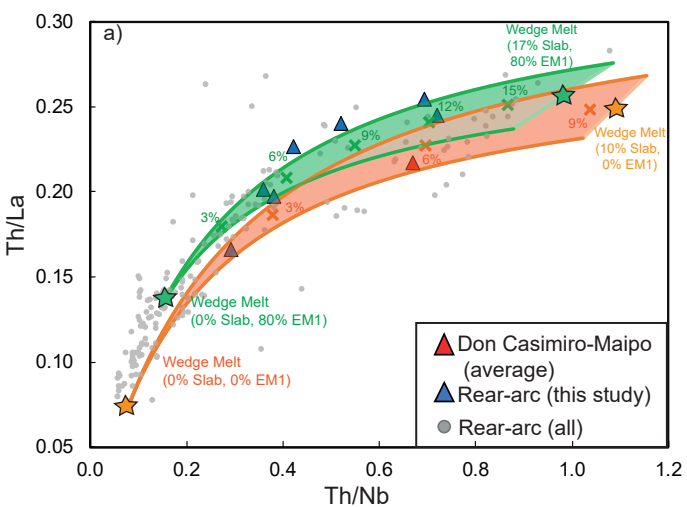


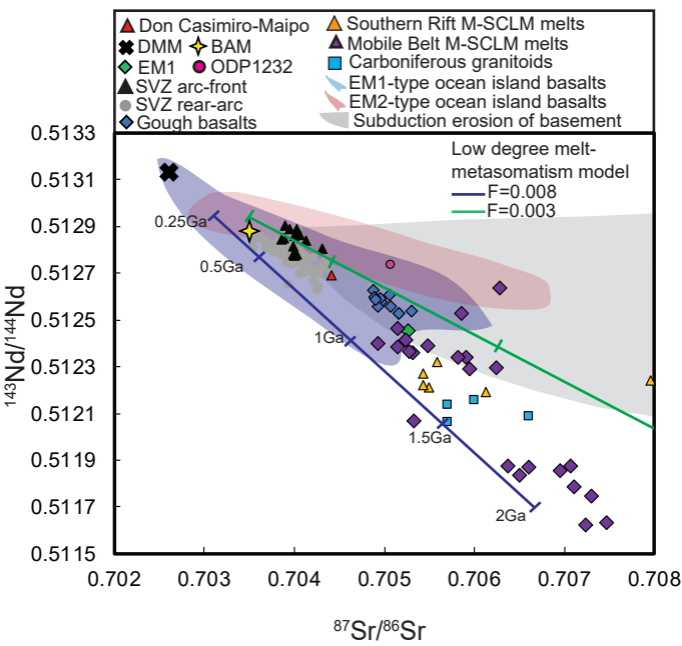
Data vs. model results for Villarrica and Don Casimiro-Maipo

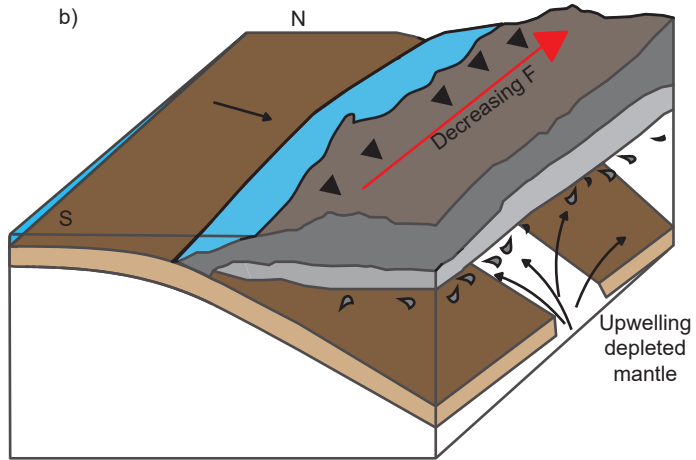
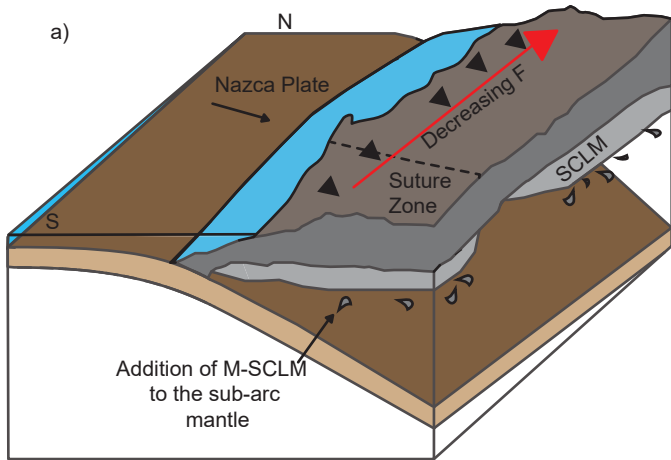


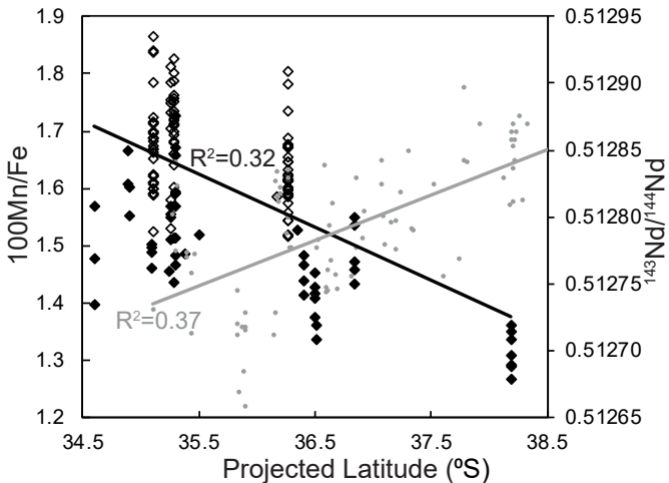
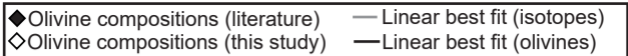
- ▲ Don Casimiro-Maipo primitive average
- ▲ Villarrica primitive average
- Isotopically plausible
- Isotopically implausible

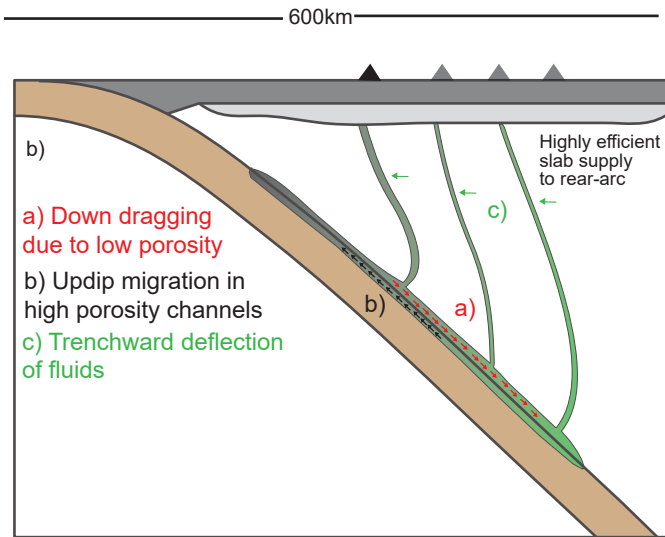
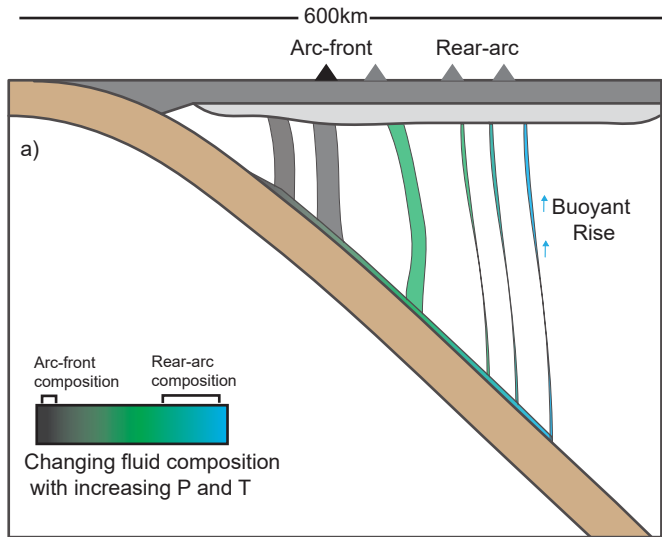












Appendix 1: Methods and Sample Details

SIA1 Data and Databases

1 Whole-rock and olivine analysis from this study is shown in Appendix 3. Compiled rear-arc
 2 and Diamante-Maipo literature data used in this study is in Appendix 4. The compilation
 3 of SVZ basement compositions is in Appendix 5.

4 SIA2 Sample Characteristics

5 Six 100 μ m sections were made for Don Casimiro-Maipo samples spanning a range of MgO
 6 contents. These were scanned using a 5MP slide scanner. Point counting was conducted in
 7 JMicroVision by overlaying a 1000 point grid on these scans. Microscope observations were
 8 made on any crystals that couldn't be identified with certainty in scans. Crystals smaller
 9 than ~ 0.05 mm were classified as matrix. Amorphous or crystalline material sufficiently
 10 distinct from the surrounding matrix that could not be identified as a mineral phase was
 classified as alteration.

Table SA1: Point counting results for Don Casimiro-Maipo samples (ordered by decreasing wt% MgO).

Sample	MgO (wt%)	Crystals (%)	Matrix (%)	Vesicles (%)	Alteration (%)
G0020315-1	6.82	11	89	0	0.1
G0020315-2	6.73	10	90	0	0.3
G0270215-1D	5.63	17	81	0	0.3
G0270215-1C	4.85	14	85	0	0.2
G0030315-4	3.87	11	72	16	0.0
G0030315-1	2.99	42	48	0	10

Table SA2: Percentage of each phenocryst phase in the crystal fraction. *The fine grained nature of these samples meant that phenocryst phases were harder to identify, so proportions are not as reliable as for other samples.

Sample	Olivine (%)	Clinopyroxene (%)	Plagioclase (%)	Oxide (%)	Orthopyroxene (%)
G0020315-1	66	34	0	0	0
G0020315-2	66	34	0	0	0
G0270215-1D*	6	15	46	33	0
G0270215-1C*	8	20	32	41	0
G0030315-4	7	5	89	0	0
G0030315-1	3	13	82	0	3

Table SA3: Description of Don Casimiro-Maipo samples in thin section.

Sample	Olivine	Plagioclase	Clinopyroxene	Matrix Textures
G0020315-1	Predominantly subhedral-anhedral 2-0.5mm grains, and smaller, <0.5mm anhedral grains. Both types form clots, and show association with clinopyroxene. Most olivines contain oxide inclusions.	No phenocrysts.	Subhedral-anhedral 2-0.5mm grains, often forming clots. Smaller, <0.5mm anhedral grains within the matrix. Some show breakdown in their cores.	Dark, fine grained matrix with white streaks of amorphous material. Needle-shaped matrix plagioclase aligns with these streaks. A few 1-2mm patches of alteration are associated with reacted olivine cores.
G0020315-2	Euhedral 1-3mm grains, subhedral 0.5-2mm clots associated with clinopyroxene, and smaller isolated <1mm anhedral grains.	No phenocrysts.	Subhedral 1-2mm grains, often associated with olivine clots. As above, some show broken down cores.	Dark, fine grained matrix, with white amorphous material in streaks. Small needle-shaped plagioclase shows alignment around large crystals. Abundant anhedral oxide grains.
G0270215-1D	Anhedral <0.2mm grains with abraded edges. These are associated with patches of small red amorphous material.	Blocky to needle-shaped plagioclase. No alignment.	Sub-anhedral, 0.3-1mm grains. These are more commonly associated with the red material than olivines.	Dark, fine grained matrix, with poorly aligned, needle-shaped plagioclase, and dispersed anhedral oxides. Patches of white, amorphous material.
G0270215-1C	Anhedral, <0.1mm grains.	Elongated needles, 20:1 aspect ratio. Aligned in matrix.	Sub-anhedral 0.3-1mm grains, associated with red amorphous material and oxide growth.	Dominated by small, aligned, needle-shaped plagioclase, with euhedral-anhedral opaque oxides.
G0030315-4	Anhedral, <1mm grains, with highly abraded edges, likely these were originally clots.	Large, 2mm+, blocky plagioclase, showing sieve textured cores (indicating rapid growth/cooling/heating).	Euhedral, 2-4mm grains, and smaller, <1mm highly abraded anhedral grains.	Highly vesicular texture. Matrix dominated by glass.
G0030315-1	A few subhedral, 1-2mm olivines. Some associated with large, 1-2mm cubic oxide phases.	Several populations of plagioclase. 1) blocky 2-4mm rectangular macrocrysts, with large fluid inclusions. 2) lath shaped 1-3mm grains, with inclusion-free cores. 3) needle shaped (<1mm) grains, with sieve textured cores.	Euhedral-subhedral, 1-2mm grains with oxide inclusions. Some are also associated with very large, 1-3mm oxide grains. Additionally, one 4mm clot of several grains and oxides is observed. In some places, clinopyroxene forms anhedral intergrowths with plagioclase, and orthopyroxene.	Extremely crystal-rich. Large areas of amorphous material within the slide are associated with large blocky plagioclase macrocrysts. Between phenocrysts, the matrix is dark and amorphous.

12 SIA3 Methodologies

13 SIA3.1 Whole Rock Chemistry

14 Sixteen samples from Don Casimiro-Maipo and seven rear-arc samples were prepared for whole-rock analysis
 15 at the University of Oxford. Arc-front lava samples were cleaned in an ultrasonic bath until the water ran
 16 clear. These were then split into 2-3cm chunks using a pneumatic rock splitter. Rear-arc samples were wet
 17 sieved, and unaltered clasts from the coarsest fraction (>2mm) were hand picked for whole rock analysis.
 18 Both sample types were crushed in a steel jaw crusher, and then powdered in an agate ball mill.

19
 20 **Major Element Analysis:** Major element analyses was conducted by using a PANalytical Axios Advanced
 21 X-ray fluorescence spectrometer at the University of Leicester, UK, following the methods of Knott et al. (2016).

22
 23 **Trace Element Analysis:** ~ 100 mg of each powder as well as reference materials BCR-2a, BHVO-2,
 24 W-2a and AGV-2, were digested in ~4ml of 7.5M HNO₃ and ~1ml of 24M HF. The samples were then
 25 evaporated and redissolved twice in ~4ml 7.5M HNO₃ to eradicate fluoride precipitates. At this stage, a
 26 sample split was made for isotopic analysis. Trace element analyses were conducted using a Perkin Elmer
 27 NexION 350D quadrupole ICP-MS for the majority of elements. An additional 1200x dilution and addition
 28 of an internal standard containing Rh, Re, and In was achieved using the ESI prepFAST system producing
 29 a 6000x solution in which to measure lower concentration elements. All prior dilutions were performed
 30 gravimetrically. Sample G0030315-4 was run every four samples, and the entire run was duplicated in reverse
 31 order to monitor drift. Drift correction and data reduction were carried out following Turner et al. (2013).
 32 Due to malfunctioning of the Prepfast system, a planned run at 60,000x dilution for higher concentration
 33 elements using the same method failed. Thus, Sr and Ba concentrations were measured using a Thermo
 34 Element 2 ICP-MS (also at the University of Oxford) at a 1,200,000x dilution (performed gravimetrically).

35 The digestion procedure, and sample homogeneity can be assessed by calculating the % difference between
 36 the measured element concentrations of two duplicates produced from the powders of this study, and two
 37 from an additional set of samples digested alongside these. Most measurements lie within 5%, suggesting
 38 that the digestion process, and samples, were reasonably homogeneous (table SA4).

39 Isotopic Analysis

40 Strontium (Sr) and neodymium (Nd) isotope analyses were performed on a Thermo Scientific Triton-series
 41 multicollector mass spectrometer at the School of Earth and Environment, University of Leeds. Eleven
 42 whole-rock powders were digested alongside those for trace element analysis, followed by subsequent drying
 43 and pick up in concentrated ultrapure HNO₃ and HCl acids. The final dried samples were diluted and
 44 centrifuged for 15 minutes at 2000 rpm. Sr and Nd were extracted by using Sr-Spec and TRU-spec resins and
 45 conventional ion-exchange chromatographic techniques. ⁸⁷Sr/⁸⁶Sr and ¹⁴³Nd/¹⁴⁴Nd ratios were normalized for
 46 mass fractionation to ⁸⁶Sr/⁸⁸Sr=0.1194 and ¹⁴⁶Nd/¹⁴⁴Nd=0.7219. Samples for Sr were loaded onto previously
 47 outgassed W filaments and samples for Nd were loaded onto previously outgassed Re filaments. Sr and Nd
 48 were analysed while the current was maintained between 3-5 V (for ⁸⁸Sr) and 0.4-0.8 V (for ¹⁴⁴Nd).

49 The average ⁸⁷Sr/⁸⁶Sr obtained from repeated measurements of NIST SRM-987 during the course of this
 50 study was 0.710271. Similarly, we measured ¹⁴³Nd/¹⁴⁴Nd=0.511837 for the LaJolla standard. Two samples
 51 (G0020315-2 and G0270215-1C) were analyzed for ¹⁴³Nd/¹⁴⁴Nd in a separate run, in which we measured
 52 ¹⁴³Nd/¹⁴⁴Nd=0.511850 for the LaJolla standard. We also successfully reproduced the published USGS
 53 standard BHVO-2 values for ⁸⁷Sr/⁸⁶Sr=0.703468 and ¹⁴³Nd/¹⁴⁴Nd=0.512995 (Weis et al., 2005). Details
 54 on the sample preparation and analytical protocols are described in Crummy et al. (2014).

55 SIA3.2 Correction of Isotopic data of this study and Literature 56 Data

57 Sr and Nd isotopes from the literature and this study were corrected to be in line with the analytical procedure
 58 used for SVZ data presented in Turner et al. (2016). Various standards were corrected to be equivalent
 59 to La Jolla=0.511858, NBS 987=0.710235 based on session averages.

Table SA4: % deviation of four duplicates ran during analysis on the "quad" (except starred elements, where % deviation is reported from the "element"). (4) represents a duplicate of G0030315-4, (1) represents a duplicate of MDZ1, 079a and B1 are samples measured in the same run, but for use in a study on the Main Ethiopian Rift. % deviation is defined as (Measurement 1-Measurement 2)/(Average of measurement 1 and 2) x 100.

	% difference (4)	% difference (1)	% difference (079)	% difference (B1)
Li	4.13	1.74	-0.97	0.35
Be	-4.52	60.2	-12.4	1.29
Sc	5.89	-27.0	-20.5	-0.72
V	2.02	-1.95	-0.65	0.15
Cr	3.02	0.41	1.14	-0.99
Ni	3.53	0.74	0.86	1.47
Cu	4.71	-3.94	-0.26	1.76
Rb	3.64	0.28	-9.66	0.30
Sr*	5.54	1.74	0.35	-5.67
Y	2.99	-3.08	-6.18	-0.94
Zr	2.12	-0.29	-0.42	0.32
Nb	3.09	0.21	-0.30	1.16
Cs	8.90	-5.49	-4.43	9.11
Ba*	6.08	3.17	3.65	-2.89
La	3.52	0.58	1.10	0.82
Ce	3.31	-1.09	0.94	0.70
Pr	4.57	0.71	2.05	0.80
Nd	3.29	3.63	-0.88	-0.53
Sm	0.00	2.17	1.35	2.23
Eu	2.21	2.20	1.55	-1.12
Gd	3.09	-2.92	-2.87	1.04
Tb	3.26	-2.17	2.29	0.91
Dy	3.83	-0.60	2.67	0.78
Ho	4.64	-2.73	-0.32	3.88
Er	2.99	4.01	-2.53	3.70
Tm	2.81	-5.67	-3.75	0.51
Yb	2.67	1.49	-0.23	1.69
Lu	1.28	1.41	-3.58	1.15
Hf	3.34	0.93	-0.87	1.40
Ta	-2.98	-0.57	1.60	-0.94
Pb	3.55	-2.14	-9.60	1.72
Th	3.48	-2.05	-17.6	-1.10
U	3.33	-0.09	0.56	-0.11

60 SIA3.3 Olivine Chemistry

61 Olivines were picked from the 1000-250 μ m grain fractions, and mounted in epoxy rings. These
62 mounts were polished and carbon coated for EMPA analysis. Analysis was conducted with
63 an accelerating voltage of 15KeV, a current of 100nA and a 10 μ m spot size. St John's Island
64 and Fayalite were run as secondary standards, with % recoveries reported in table SA5.

65 LA-ICP-MS analysis was conducted at the University of Cambridge. Three instrument
66 runs were performed over two days. The run conditions were 20Hz, 80 μ m, 9.5J/cm², 0.8L/min
67 of gas flow for He and Ar. Where possible, three spots were placed in the centre of the olivine,
68 with no overlap. For very small grains, only 2 spots were placed, as it is preferable to have
69 fewer spots nearer the centre than more spots towards the grain edges, due to the reasonably
70 high diffusivity of elements of interest to this study. To allow drift correction, 3 spots on each of

71 NISTSRM612, NISTSRM610, 06SGOL03 (inhouse olivine standard) and BD4074OL-7 (a San
 72 Carlos olivine) were run every 30 analyses. ^{29}Si was used as an internal standard, with values
 73 obtained from EMPA grain averages. Signals were selected using Glitter Processing software,
 74 with normalization to NISTSRM612 via a quadratic drift correction. This was effective at
 75 removing drift, as determined by observing the stability of NISTSRM610, 06SGOL03 and
 76 BD4074OL-7 following this correction. Multiple secondary standards were run to assess the
 77 accuracy of the measurement for elements of interest (NISTSRM610, NISTSRM614, BCR-2G).
 78 Measurement of inhouse olivines O6SGO103 and BD407OL-7 provided an excellent assessment
 79 of the success of the drift correction performed on glass standards. Elements of interest in this
 80 study drifted by less than 7%. Although Mn and Ni recovery on glass standards were good,
 81 these elements were recovered more poorly on BCR-2G. This, and the fact that previous
 82 studies in this area have used EMPA Ni and Mn data, resulted in us choosing to use EMPA
 83 data for consistency, as most of the peridotite-pyroxenite ratios involve normalization to Fe
 84 (which is reported from EMPA). Detection limits, and 1 sigma uncertainties calculated from
 85 Glitter for a representative sample (MDZ2) are shown in table SA6.

Table SA5: Peak count times, and calibration materials used. % recovery calculated below is defined as Measured Average/Published Average x 100. Where no published value exists for a standard, - is shown. Detection limits are reported from 9 spots on MDZ8. These are assumed to be representative of the analysis as a whole.

	Mn	Fe	Mg	Si	Ca	Ni
Peak count times (s)	20	30	20	20	70	70
Calibration material	Mn metal	Andradite	MgO	Albite	Wollastonite	Ni metal
% Rec Fayalite	97.7	94.2	-	99.6	97.0	-
% Rec St Johns Island Olivine	106.1	96.1	99.6	99.2	-	90.1
Detection limit (ppm)	173	197	173	98	74	137

Table SA6: Minimum (99% Confidence) detection limits (ppm), and 1 sigma uncertainties (ppm) for all spots on MDZ2, taken as representative for the analysis as a whole. The mass in brackets represents the isotope measured on the ICP-MS.

Element	MDL	1 σ uncertainty
Li(7)	0.115	0.151
Na(23)	1.121	6.92
Al(27)	0.318	39.3
P(31)	13.76	47.3
Ca(43)	133	192
Sc(45)	0.062	0.412
Ti(47)	0.551	18.4
V(51)	0.043	0.504
Cr(53)	0.578	56.0
Mn(55)	0.136	88.4
Co(59)	0.049	7.91
Ni(60)	0.171	191
Cu(65)	0.351	0.416
Zn(66)	0.373	10.1
Ga(69)	0.042	0.049
Ge(72)	0.370	0.208
Y(89)	0.037	0.025
Zr(90)	0.033	0.052
Nb(93)	0.035	0.021

Table SA7: % recovery of NISTSRM610 (average of 3 spots). (x,y) refers to when this secondary standard was run, x referring to the instrument run (1-3), and y to the order of measurement within a given run. These values were used to check the success of the quadratic drift correction. Across the three instrument runs, most elements drift by less than 10%.

Element	(1,1)	(1,2)	(1,3)	(1,4)	(1,5)	(2,1)	(2,2)	(2,3)	(2,4)	(3,1)	(3,2)	(3,3)	(3,4)	AVERAGE
Li(7)	98.0	105.5	103.7	106.7	105.9	107.3	104.3	101.1	103.6	108.0	99.6	96.8	98.2	103.0
Na(23)	98.2	105.7	107.0	106.1	105.9	105.9	104.9	101.4	103.9	105.0	103.0	101.1	102.1	103.9
Al(27)	102.3	105.5	105.9	106.2	107.8	108.3	104.2	104.9	107.3	105.6	107.2	103.5	104.9	105.7
P(31)	107.8	105.2	99.7	130.9	194.5	100.5	103.9	101.0	100.5	125.0	113.1	117.6	133.9	118.0
Ca(43)	95.9	103.7	100.6	106.7	107.3	105.2	102.5	99.2	102.2	105.2	100.1	99.5	104.5	102.5
Sc(45)	98.7	109.1	108.0	109.8	108.8	110.2	110.9	105.6	108.9	108.5	106.7	108.0	109.6	107.9
Ti(47)	115.2	120.8	116.9	120.0	119.0	125.1	128.7	124.5	125.5	125.3	125.9	122.8	125.4	122.7
V(51)	95.7	101.9	100.1	105.2	105.8	104.8	102.6	100.1	105.1	105.9	101.7	99.9	103.7	102.5
Cr(53)	103.4	107.7	109.4	113.6	119.5	120.7	115.9	112.1	115.1	114.1	111.4	112.7	116.7	113.2
Mn(55)	94.6	100.0	100.0	103.7	102.4	105.1	100.2	99.0	103.5	104.9	97.1	96.1	97.7	100.3
Co(59)	95.5	103.0	101.7	103.7	100.8	104.2	102.0	98.9	104.3	103.6	101.0	100.3	103.4	101.7
Ni(60)	92.1	100.9	99.8	103.7	99.9	105.6	100.1	98.2	100.0	104.3	101.8	100.5	102.2	100.7
Cu(65)	89.9	98.8	97.3	100.1	97.5	100.5	98.4	94.9	99.0	100.1	96.0	95.9	97.6	97.4
Zn(66)	98.5	104.1	102.3	108.8	110.2	111.1	104.4	100.1	106.6	109.9	106.4	104.1	102.9	105.3
Ga(69)	92.2	97.7	96.5	101.1	101.5	101.7	99.0	97.2	99.4	101.4	98.9	98.3	100.8	98.9
Ge(72)	81.5	86.7	85.7	89.1	88.8	92.4	89.0	85.6	86.6	92.0	87.5	87.8	89.8	87.9
Y(89)	93.1	102.1	99.8	102.8	102.1	104.0	102.9	100.5	100.3	102.5	101.4	101.8	103.8	101.3
Zr(90)	89.8	95.9	94.6	97.9	98.1	98.6	98.5	94.6	95.4	97.5	96.8	96.0	98.7	96.3
Nb(93)	92.8	99.9	98.9	102.4	101.7	102.2	102.2	98.1	100.2	102.9	99.9	99.2	101.1	100.1

Table SA8: % recovery of BCR-2G, using averages from 3 spots, and % recovery of NISTSRM614. The % recovery for NISTSRM614 is not shown for the first run. These were the first spots ran by the laser, and it has been shown that the system takes a few spots to warm up and settle after switching from solution mode to laser mode.

Element	(1,1)	(2,1)	(2,2)	(3,1)	(3,2)	BCR-2G Average	(2,1)	(3,1)	NISTSRM614 Average
Li(7)	100.2	104.5	101.7	105.8	94.6	101.4	84.4	103.7	94.1
Na(23)	96.2	99.1	97.0	101.4	96.9	98.1	105.5	103.1	104.3
Al(27)	103.8	103.4	99.9	104.6	103.3	103.0	106.6	106.3	106.4
P(31)	101.3	84.9	86.8	108.4	120.1	100.3	268.2	260.0	264.1
Ca(43)	99.0	97.9	98.9	101.1	99.1	99.2	106.2	103.7	105.0
Sc(45)	97.5	102.1	96.4	100.8	99.9	99.3	217.1	185.9	201.5
Ti(47)	107.3	108.4	105.2	110.9	106.3	107.6	122.1	101.3	111.7
V(51)	97.6	100.1	101.1	102.8	99.6	100.2	109.7	99.9	104.8
Cr(53)	93.2	104.4	92.9	97.1	101.1	97.7	94.8	113.0	103.9
Mn(55)	92.4	96.6	94.9	98.5	90.0	94.5	105.6	89.7	97.7
Co(59)	99.0	97.8	97.0	97.9	96.2	97.6	92.6	95.0	93.8
Ni(60)	89.4	86.9	83.8	90.2	86.5	87.4	107.9	71.8	89.8
Cu(65)	71.0	72.5	67.5	71.1	69.6	70.3	88.8	109.0	98.9
Zn(66)	121.5	134.0	127.4	134.9	120.7	127.7	91.4	89.2	90.3
Ga(69)	111.6	117.1	109.2	118.4	114.5	114.2	96.9	93.9	95.4
Ge(72)	99.6	112.9	95.6	101.1	102.4	102.3	86.3	110.8	98.5
Y(89)	87.3	90.0	81.9	90.6	89.1	87.8	102.0	99.4	100.7
Zr(90)	84.5	87.0	78.3	87.7	86.3	84.7	90.3	91.6	90.9
Nb(93)	88.6	91.6	86.6	91.0	90.2	89.6	93.7	99.3	96.5

86 SIA4 Mantle Melting Model Details

87 As discussed in the text, this study uses an updated version of the model of Turner and
88 Langmuir (2015b). Below, the justification of various inputs to the model are discussed. The
89 updated Matlab scripts ADD_SLAB.m, ADD_SLAB_HOTP.m and ModeMelt_Hydrous.m
90 have been uploaded into the supplementary information.

91 SIA4.1 Model Partition Coefficients

92 **Hydrous Partition Coefficients for Mantle Melting:** This study utilizes hydrous
93 partition coefficients and mantle modes from Turner and Langmuir (2015b; detail in their
94 supplement). However, we slightly updated the partitioning behaviour of several elements:
95

96 1) The bulk partition coefficient of Eu is obtained by a log extrapolation from those of Sm and
97 Gd:

$$98 \quad Kd_{Eu} = (Kd_{Sm} * Kd_{Gd})^{0.5}$$

99 correcting an error in Turner and Langmuir (2015b).

100 2) The partition coefficient of Hf is assumed to be equal to that of Sm.

101 3) The partition coefficient of Zr is approximated as:

$$102 \quad Kd_{Zr} = (Kd_{Nd} * Kd_{Sm})^{0.5}$$

103 **Hydrous Partition Coefficients for slab melting:** As above, this study uses slightly
 104 adapted partition coefficients for slab melting to those in Turner and Langmuir (2015b).
 105 These lie within the limits of experimental values (figure SA1). The partition coefficients for
 106 the LREE (La, Ce, Nd, and Sm) were reduced by 40% to reflect the hotter slab underneath
 107 Don Casimiro-Maipo (inline with experimental high temperature partitioning results; figure
 108 SA1). Additionally, the partition coefficients of Zr and Hf were reduced, and 70% of Cs
 109 was assumed to be lost to the forearc.

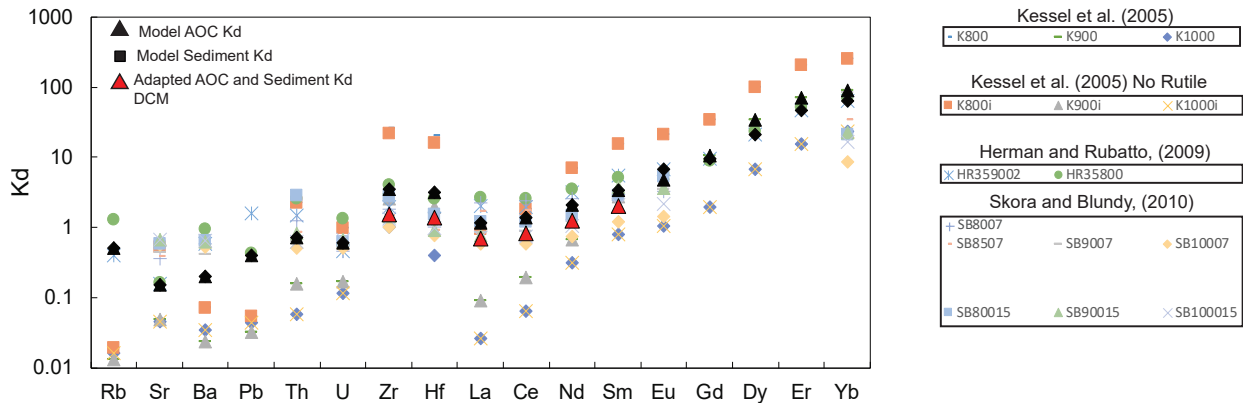


Figure SA1: Slab melting partition coefficients lie within experimental values for 800-1000°C.

110 SIA4.2 Model End-Members

111 **"Ambient Andean Mantle" (Depleted Mantle End-Member):** The isotopic composition
 112 of the depleted mantle end member was set to $^{87}\text{Sr}/^{86}\text{Sr}=0.70355$ and $^{143}\text{Nd}/^{144}\text{Nd}=0.512871$,
 113 the isotopic composition of sample 126171 of Soager et al. (2013) following the isotopic
 114 correction discussed above. This sample lies at the depleted end of the rear-arc array,
 115 and thus reflects the composition of the Andean mantle prior to the addition of EM1
 116 enrichment. For trace element modelling, the depleted mantle end-member is DMM of
 117 Workman and Hart (2005).

118 **AOC:** The subducting Nazca plate has Pacific affinities. Trace element concentrations
 119 were obtained from melting of N-MORB (Gale et al., 2013) at 876°C, $F=0.3$. The isotopic
 120 composition of AOC was set to $^{87}\text{Sr}/^{86}\text{Sr} = 0.7035$, $^{143}\text{Nd}/^{144}\text{Nd} = 0.5130$.

121 **Sediment:** The trace element composition of the sediment end-member was obtained from 33
 122 samples of ODP1232 (c.f. Turner et al., 2017). To produce an envelope of model results for trace
 123 elements and isotopes, one standard deviation of measured samples were added and subtracted
 124 to the mean. Three outliers were discarded based on their anomalously high Sr isotope ratios.

125 **Enriched EM1 end-member:** Enrichment at Gough represents a mix of M-SCLM, and
 126 ambient mantle. The isotopic signature of recycled M-SCLM depends on the storage time
 127 (Turner et al., 2017). As several samples within this study have signatures more enriched
 128 than Gough, we use the isotopic composition of a sample from Pitcairn (57DS9; Stracke et
 129 al., 2003) as the EM1-like isotopic end member. This lies at the enriched end of the field

130 enclosing EM1-type ocean island basalts. The trace element concentration was obtained
 131 from the inversion of Turner et al. (2017), with a few changes:

132 1) the bulk Eu partition coefficient was set at:

$$133 \quad Kd_{Eu} = (Kd_{Sm} * Kd_{Gd})^{0.5}$$

134 correcting an error in Turner et al. (2017) where it was set at 0.

135 2) The Zr concentration in Gough primary melts was adjusted to the standard EM1 value
 136 $Zr/Hf = 45$.

137 3) Zr partition coefficients were extrapolated from Salters and Longhi (1999).

138 4) Nb and Ta partition coefficients were taken as $Kd_{La}/3$, based on ratios from Workman and
 139 Hart (2005).

Table SA9: Gough mantle source composition used in this study compared to that of Turner et al. (2017; T2017).

	Eu	Zr	Nb	Ta
This study	0.130	6.70	0.403	0.024
T2017	0.0234	11.47	0.472	0.028

140 SIA5 References

141 Crummy, J., Savov, I.P., Navarro-Ochoa, C., Morgan, D., Wilson, M., 2014. High-K mafic Plinian eruptions of
 142 Volcán de Colima, México, *Journal of Petrology*, 55 (10). pp.1-18.

143
 144 Kessel, R., Schmidt, M.W., Ulmer, P. and Pettko, T., 2005. Trace element signature of subduction-zone fluids,
 145 melts and supercritical liquids at 120–180 km depth. *Nature*, 437(7059), pp.724-727.

146
 147 Knott, T.R., Branney, M.J., Reichow, M.K., Finn, D.R., Coe, R.S., Storey, M., Barfod, D. and McCurry, M.,
 148 2016. Mid-Miocene record of large-scale Snake River-type explosive volcanism and associated subsidence on
 149 the Yellowstone hotspot track: The Cassia Formation of Idaho, USA. *Bulletin*, 128(7-8), pp.1121-1146.

150
 151 Roduit, N. JMicroVision: Image analysis toolbox for measuring and quantifying components of high-definition
 152 images. <http://www.jmicrovision.com> (accessed 4th January 2017).

153
 154 Salters, V. and Longhi, J. (1999). Trace element partitioning during the initial stages of melting beneath
 155 mid-ocean ridges. *Earth and Planetary Science Letters* 166: 15-30. doi: 10.1016/S0012-821X(98)00271-4.

156
 157 Turner, S.J., Izbekov, P. and Langmuir, C., 2013. The magma plumbing system of Bezymianny Volcano:
 158 Insights from a 54 year time series of trace element whole-rock geochemistry and amphibole compositions.
 159 *Journal of Volcanology and Geothermal Research*, 263, pp.108-121.

160
 161 Weis, D., Kieffer, B., Maerschalk, C., Pretorius, W., Barling, J. 2005. High-precision Pb-Sr-Nd-Hf isotopic
 162 characterization of USGS BHVO-1 and BHVO-2 reference materials. *Geochemistry Geophysics Geosystems*, 6,
 163 Q02002.

Appendix 2

SIB1 Evidence for Olivine Addition

EMPA analysis indicates that Don Casimiro-Maipo olivines lie significantly below the olivine-whole rock equilibrium line (Figure SB1a), indicating excess olivine accumulation. The two most primitive samples, which are from the basal section of Maipo volcano, can be related to the otherwise coherent liquid line of descent among the Diamante Caldera samples by the addition of 7 wt. % Fo 81 olivine (figure SB1b-d.). All samples have phenocrysts of olivine and clinopyroxene, so this trend is not consistent with fractionation of these two phases together. Olivine may have been accumulated from a mush pile produced by fractionation before clinopyroxene appears on the liquidus. This serves as an excellent example of the importance of utilizing individual mineral analyses in conjunction with whole-rock data when interpreting subtle geochemical variations within individual volcanic groups. While it is tempting to represent the parental composition of a volcanic group using the most olivine-phyric samples (6-7vol% olivine, in this case), such samples can often have more complicated petrogenetic histories.

SIB2 Changes in Slab Conditions Inferred from Zr-Hf Anomalies

Using Hf/Sm as a proxy, we find that rear-arc and most arc-front volcanics have a similar range of Zr-Hf values, but Don Casimiro-Maipo has a less pronounced Zr-Hf anomaly (figure SB2). The smaller Hf/Sm (and thus Zr-Hf anomaly) at Don Casimiro-Maipo may reflect the fact that the slab is slightly hotter, which causes residual slab zircon to become more soluble in the slab melt (Hirai et al., 2018).

SIB3 Evidence for AFC processing

As mentioned briefly in the main text, when samples from the entire Diamante-Maipo caldera complex are considered, the correlations between $^{87}\text{Sr}/^{86}\text{Sr}$ and $^{143}\text{Nd}/^{144}\text{Nd}$ and indices for fractionation and assimilation (MgO and Eu/Eu^*) provide strong evidence for AFC (figure SB3)

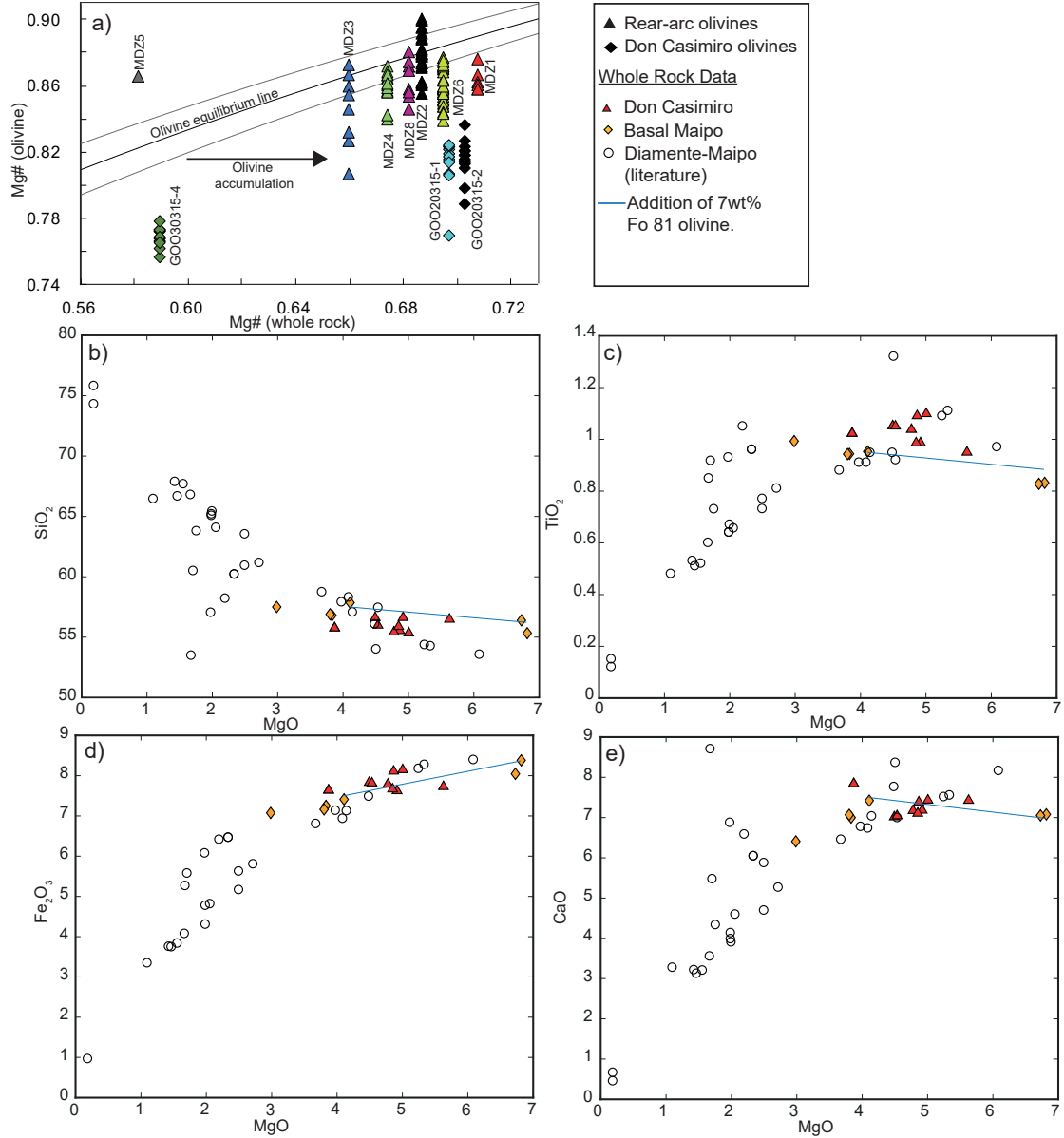


Figure SB1: a) Don Casimiro-Maipo samples show strong evidence for olivine addition, with olivine compositions plotting below an equilibrium line calculated using Roeder and Emslie (1970), $K_d=0.3\pm 0.03$, assuming whole-rock $Fe^{3+}/Fe_T=0.3$ (Holm et al., 2016). Most rear-arc olivines plot near to or below the equilibrium line, suggesting minor olivine addition (assuming whole-rock $Fe^{3+}/Fe_T=0.15$, Søger et al., 2015b). b-d) Addition of 7 wt% Fo 81 olivine from more evolved Maipo samples produces a good match to the most primitive samples, showing that their high MgO contents are spurious. Diamante-Maipo whole-rock data literature data used in this study is from Hickey et al. (1986), Futa and Stern, (1988), Sruoga et al. (2005), Holm et al. (2014) and Hickey et al. (2016).

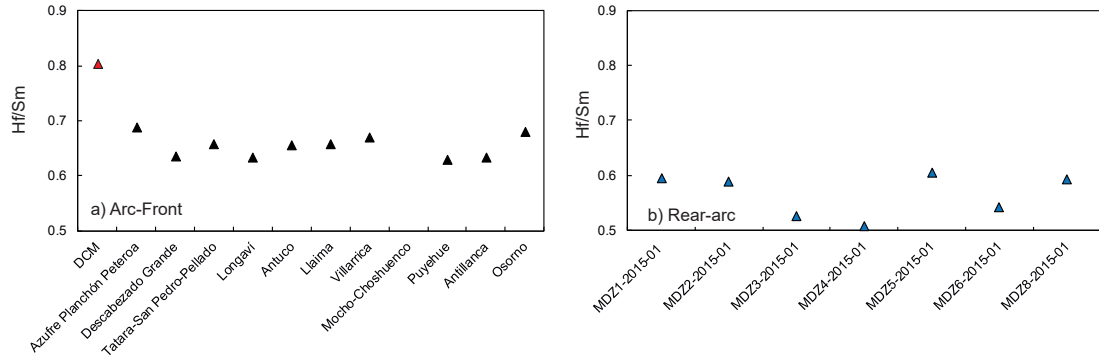


Figure SB2: a) Don Casimiro-Maipo has a significantly different Hf/Sm signature to the rest of the SVZ (data for other centers from Turner et al., 2016). b) Rear-arc centers of this study have similar Hf/Sm ratios to the SVZ arc-front as a whole.

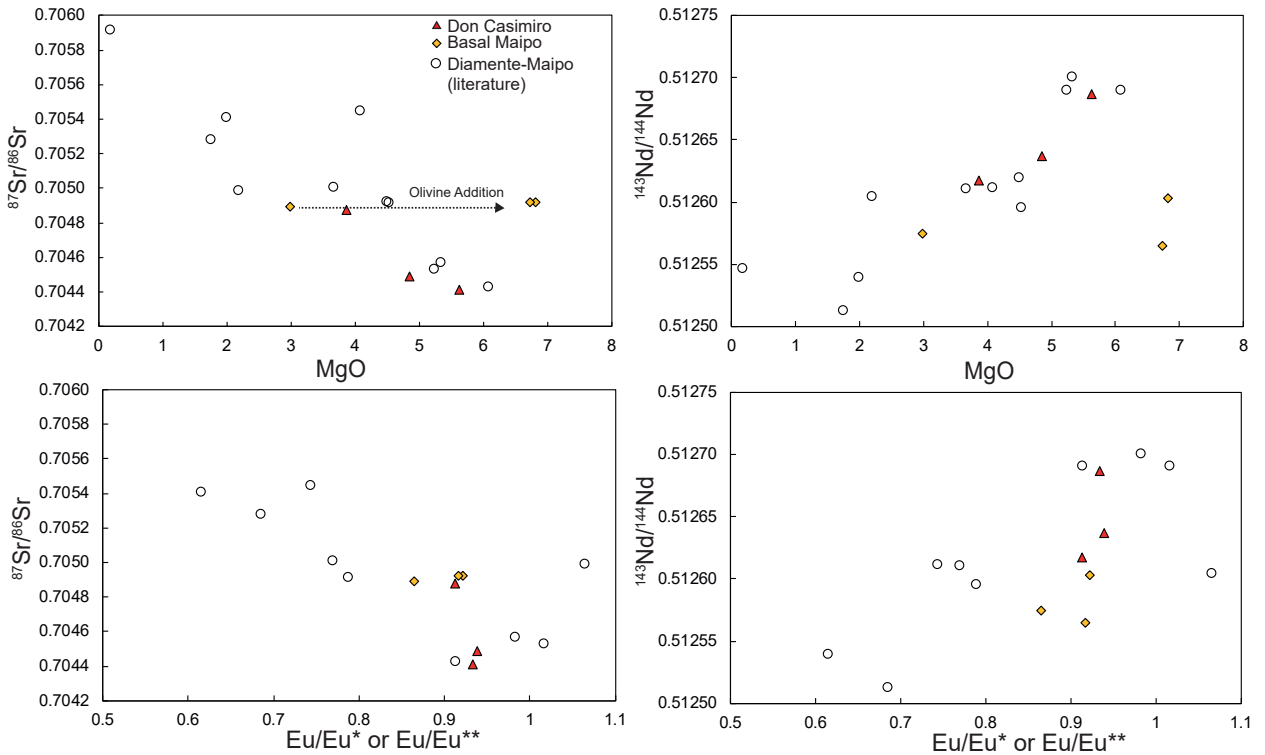


Figure SB3: Within the Diamante-Maipo Caldera, isotopic enrichment increases with assimilation and fractionation. The signal of olivine addition for the two most primitive Maipo samples is also clear.

SIB4 Olivine Chemistry

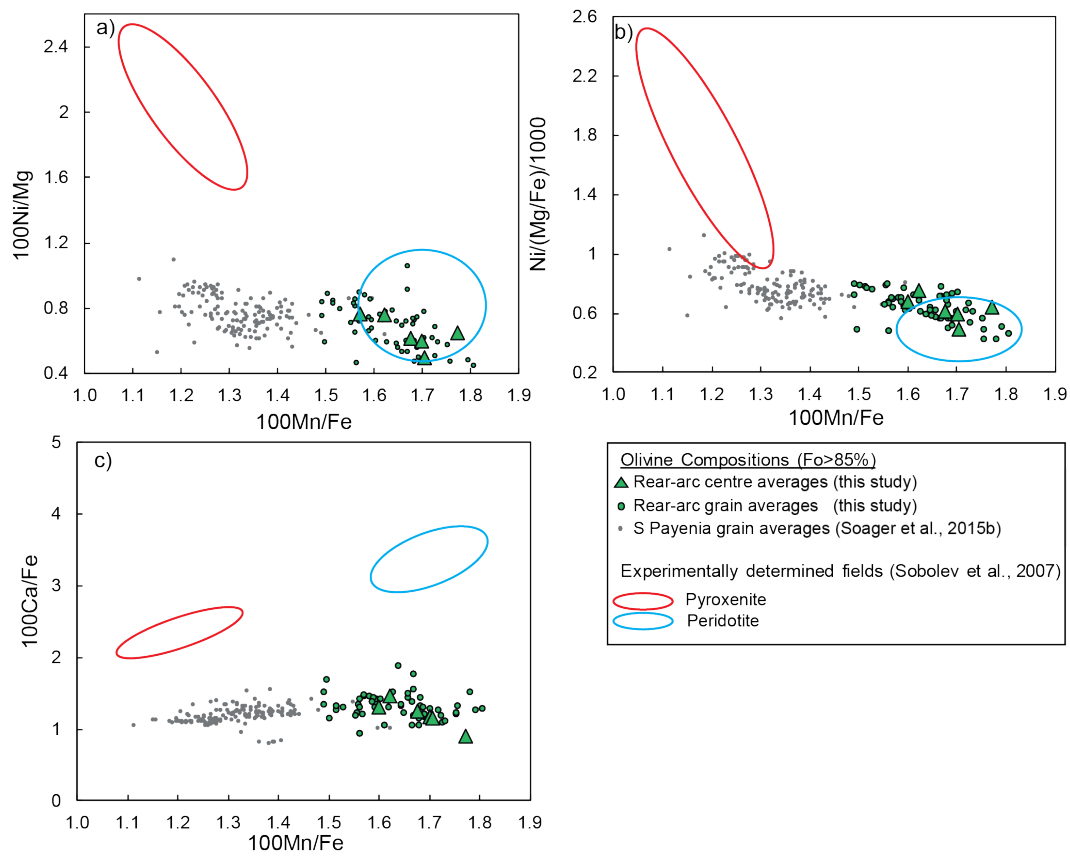


Figure SB4: Olivine analysis of this study lie within, or close to the peridotite field from Sobolev et al. (2007). Additionally, they clearly lie at more peridotitic values than the results of Soager et al. (2015b), despite showing significantly higher isotopic enrichment. While in b), the samples of Soager et al. (2015b) trend towards the pyroxenite field of Sobolev et al. (2007), in a) and c) they do not.

References

Roeder, P.L. and Emslie, R., 1970. Olivine-liquid equilibrium. Contributions to mineralogy and petrology, 29(4), pp.275-289.